Analysis of the intensity profile of a VCSEL with Hermite-Gauss modes

Robert Varano

Department of Electrical and Computer Engineering
McGill University
Montréal, Québec, Canada

November 2002

A thesis submitted to the Faculty of Graduate Studies and Research in partial fulfillment of the requirements of the degree of Master of Engineering

Your file Votre référence
ISBN: 0-612-88394-9
Our file Notre référence
ISBN: 0-612-88394-9

Abstract

Vertical cavity surface emitting lasers (VCSELs) are increasingly being used in various photonic applications. In order to design an optical system which will transmit the light emitted by a VCSEL it is necessary to model the intensity profile. The purpose of this thesis is to apply a method of extracting the modal content from an intensity profile assumed to be composed of Hermite-Gauss modes. This will be done for both the simulated output of a VCSEL and for experimentally measured intensity profiles. It will be demonstrated that the method will produce an accurate model for a VCSEL output which is close to being ideally Hermite-Gauss. Two experimental setups used to measure the intensity profiles will be presented. The first uses a scanning near-field optical microscope (SNOM) to measure the intensity near the surface of the VCSEL. In the second setup the intensity is measured at the output of a two-lens system used to image the beam waist.

Sommaire

Les lasers à cavité verticale avec émissions de surface (VCSELs) sont utilisés dans plusieurs applications photoniques. Pour créer un système optique qui va transmettre la lumière émise par un VCSEL, il est nécessaire d'obtenir un modèle de l'intensité. L'objectif de cette thèse est d'appliquer une méthode pour extraire les modes d'un faisceau laser que l'on croit être composé de modes Hermite-Gauss. Ceci est fait pour un faisceau laser simulé et pour un faisceau laser mesuré expérimentalement. Il est démontré que la méthode produit un modèle précis pour un faisceau laser qui est fortement Hermite-Gauss. Deux systèmes optiques qui ont été utilisés pour mesurer l'intensité sont présentés. Le premier système utilise un SNOM pour mesurer l'intensité proche de la surface du laser. Dans le deuxième système, l'intensité est mesurée à la sortie d'un relais de deux lentilles.

Acknowledgements

I would like to thank my supervisor Prof. Andrew G. Kirk for his guidance, particularly with respect to this project but also for the guidance he provided since I first entered the Photonics Systems Group at McGill University as a summer student.

I also thank Camille-Sophie Brès and Carole Haddad for their many months of work with the SNOM, in particular over the summer of 2002, and Rittu Sehgal who helped them test it during the 2002 winter semester.

The use of the SNOM was made possible by Prof. Peter Grütter of the McGill University Physics department and the students working under his supervision.

I had the opportunity over the course of my studies to get to know many people. I wish to extend my thanks to the professors and students of the Photonics Systems Group. In particular I would like to thank Xuyen Dai Hoa, Alan Li, Vikas Sharma, and Camille Brès and also my electrical engineering colleagues André Auclair and Patrick Mitran.

I also thank my parents. They have given me a lot. In particular, they always gave me the opportunity to pursue my academic interests.

I acknowledge the National Science and Engineering Research Council (Canada) for the postgraduate scholarship (PGS A).

TABLE OF CONTENTS

1. Introduction 1
1.1 Motivation and objectives of thesis 1
1.2 Thesis organization 2
1.3 References 2
2. Literature Review 4
2.1 Introduction 4
2.2 Vertical cavity surface emitting lasers (VCSELs) 4
2.2.1 VCSEL structure and advantages 4
2.2.2 Longitudinal and transverse modes of a VCSEL 6
2.3 Scanning near-field optical microscopy (SNOM) 8
2.4 Conclusion 9
2.5 References 10
3. Multi-transverse mode laser output characterization 12
3.1 Introduction 12
3.2 Gaussian beam model 12
3.3 Hermite-Gauss and Laguerre-Gauss functions 15
3.4 M^2 factor 19
3.5 Conclusion 22
3.6 References 22
4. Theoretical basis for the extraction of HG modes 24
4.1 Introduction 24
4.2 The method presented by Gori et al 25
4.3 Performing the analysis in one-dimensional and two-dimensional discrete space .. 26
4.4 One transverse dimensional modal extraction by taking a cross-section 30
4.5 One transverse dimensional modal extraction with integration 31
4.6 Variation of the modal content due to calculation error 33
4.7 Two transverse dimensional modal evaluation 35
4.8 Properties of the measured data and their effect on calculation accuracy 38
4.9 Determination waist parameter ω_0 40
4.10 Determination of the M^2 factor 44
4.11 Conclusion 45
4.12 References 45
5. Experimental SNOM setup 47
5.1 Introduction 47
5.2 Beam sampling setup 47
5.2.1 SNOM 49
5.2.2 Piezo-control/data acquisition system 50
5.2.3 Current source 50
5.2.4 Power meter 50
5.2.5 VCSEL 51
5.3 Measured data 54
5.4 Conclusion 57
5.5 References 58

6. Extraction of HG modes from experimental data acquired by SNOM 59
6.1 Introduction 59
6.2 Modeling of a VCSEL's output 60
6.2.1 Cross-sectional method 60
6.2.2 Integration method 70
6.2.3 Two transverse dimensional method 72
6.3 Conclusion 74
6.4 References 74
7. Modal extraction using a two-lens system 75
7.1 Introduction 75
7.2 VCSEL properties 76
7.3 Evaluation of the M^2 factor and the modified beam waist ω_0' 77
7.4 Modal extraction 80
7.5 Conclusion 84
7.6 References 85
8. Conclusions 86

LIST OF FIGURES

Figure 2.1: The structure of a VCSEL. 5
Figure 3.1: Plot of the intensity function vs. radial distance from the optical axis. The value of the beam waist radius is $\omega_0 = 4\mu m$. 13
Figure 3.2: Plots of the first three Hermite-Gauss functions (G_0,G_1, G_2). The value of the beam waist radius is $\omega_0 = 4\mu m$. 17
Figure 3.3: Plots of the FFTs of the first three Hermite-Gauss functions (G_0,G_1, G_2). The results are Hermite-Gauss functions of the same order as the initial functions. 18
Figure 3.4: Plots of the FFTs of the squares of the first three Hermite-Gauss functions (G_0^2,G_1^2, G_2^2). The results are Laguerre-Gauss functions of the same order as the initial functions. 18
Figure 4.1: Surface plot of the intensity of $BEAM_1$. 28
Figure 4.2: Plot of the beam radius vs. distance on the optical axis. 28
Figure 4.3: a) The x cross-section of $BEAM_1$. b)The difference of $BEAM_1$ and the evaluated model. The error is very small, thus plots of $BEAM_1$ and the model are visually indistinguishable. 31
Figure 4.4: a) $BEAM_1$ after integration in y. b)The difference of $BEAM_1$ and the evaluated model. The error is very small. 33
Figure 4.5: Variation of the modal content due to calculation error as the beam becomes larger and is clipped. 34
Figure 4.6: x-cross section of a beam with 3.3% of the power content clipped. 34
Figure 4.7: x cross-section of $BEAM_1$ at the location of the waist. 36
Figure 4.8: The surface plot of the difference between $BEAM_1$ and the calculated 2D model. 37
Figure 4.9: The calculated modal coefficients change due to beam clipping as the sampled beam becomes larger. 38
Figure 4.10: The portion of the FFT of $BEAM_1$ (64x64) from 0 to π which is used to evaluate the modal content. The low resolution of $BEAM_1$ causes this FFT to lack sufficient detail to allow modal extraction. 39
Figure 4.11: The portion of the FFT of $BEAM_1$ (512x512) from 0 to π which is used to evaluate the modal content. The FFT is accurate and modal extraction is possible. ..40
Figure 4.12: Plot of the variance of $Beam_1$ vs. position on the optical axis. The result is a parabola.. 41
Figure 4.13: Effect on the modal coefficients if the incorrect beam waist is used. The correct values of the coefficients are found only when ω_0 for the basis functions is correct (i.e. $4\mu m$). 43
Figure 4.14: Surface plot of the error when $\omega_0=3.5\mu m$.. 43
Figure 4.15: Surface plot of the error when $\omega_0=4.5\mu m$.. 44
Figure 5.1: Schematic of the experimental setup used to measure the near-field intensity profiles of the VCSEL. 48
Figure 5.2: The aluminum coated fiber. The end has been etched in hydro-fluoric acid to produce a sharp tip. 49
Figure 5.3: The fiber is glued on a fiber holder which is then mounted onto the piezo tube. 49

Figure 5.4: The SNOM and the VCSEL mounted, aligned and ready for a scan. 50
Figure 5.5: The Newport 2823-C power meter with fiber attached connector/photo-detector. 51
Figure 5.6: VCSEL mounted on a PCB. 51
Figure 5.7: Measured current vs. voltage 53
Figure 5.8: Measured power vs. current. 53
Figure 5.9: The SNOM fiber is positioned for a scan of the VCSEL. 54
Figure 5.10: Intensity profile at I = 4mA. a) angled view and b) top view. 54
Figure 5.11: Intensity profile at I = 5mA. a) angled view and b) top view. 55
Figure 5.12: Intensity profile at I = 10mA. a) angled view and b) top view. 55
Figure 5.13: Intensity profile at I = 12mA. a) angled view and b) top view. Note that the intensity is not to the same scale as the previous 3 plots because the z-position is different for 12mA, than for the other currents. 56
Figure 6.1: a) x cross-section of the beam and the evaluated model for z-position z_1. b) The error was computed by subtracting the cross-section and the model. 62
Figure 6.2: a) y cross-section of the beam and the evaluated model for z-position z_1 . b) The error was computed by subtracting the cross-section and the model. 63
Figure 6.3: a) x cross-section of the beam and the evaluated model for z-position z_1. b) The error was computed by subtracting the cross-section and the model. 65
Figure 6.4: a) y cross-section of the beam and the evaluated model for z-position z_1. b) The error was computed by subtracting the cross-section and the model. 66
Figure 6.5: x cross-section of the beam and the evaluated model for z-position z_1. b) The error was computed by subtracting the cross-section and the model. 67
Figure 6.6: y cross-section of the beam and the evaluated model. b) The error was computed by subtracting the cross-section and the model. 68
Figure 6.7: cross-section of the beam and the evaluated model for z-position z_2. b) The error was computed by subtracting the cross-section and the model. 69
Figure 6.8: cross-section of the beam and the evaluated model for z-position z_2. b) The error was computed by subtracting the cross-section and the model. 70
Figure 6.9: Comparison of the cross-sections of beam and the evaluated model in (a) x and (b) y. 72
Figure 6.10: Difference of the actual beam and the model. 73
Figure 7.1: The VCSEL array and the first lens in the lens relay system. 76
Figure 7.2: Current vs. voltage. 76
Figure 7.3: Power vs. current. 77
Figure 7.4: Schematic of the setup used to measure the variance of the beam in order to evaluate M^2 and ω_0. 78
Figure 7.5: A new beam waist is created by the 2-lens system. The BEAMSCAN device at the output of the second lens is used to measure the variance of the modified beam. 79
Figure 7.6: The variance was sampled at 15 z-positions around the beam waist. The z-distance is measured from the location of the new waist. 79
Figure 7.7: The setup used to measure the VCSEL emission. 80
Figure 7.8: The setup used to acquire the intensity cross-section along the x-axis. 81
Figure 7.9: a) x cross-section of the beam and the evaluated model for z-position 1mm. b) The error was computed by subtracting the cross-section and the model. 82

Figure 7.10: a) x cross-section of the beam and the evaluated model for z-position 4mm. b) The error was computed by subtracting the cross-section and the model. 83
Figure 7.11: a) x cross-section of the beam and the evaluated model for z-position 1mm. b) The error was computed by subtracting the cross-section and the model. 84

LIST OF TABLES

Table 3.1: The first six Hermite and Laguerre polynomials. 17
Table 4.1: The content returned by the integration method. Although this detects all modes it is not possible to distinguish the modes individually. 32
Table 4.2: Comparison of the actual modal coefficients to the calculated modal coefficients at the waist. 36
Table 4.3: Modal content as affected by array size. 39
Table 5.1: Principle characteristics of the VCSEL (HFE4080-321) as indicated on the device specification sheet provided by Honeywell. 52
Table 6.1: Modal content in x for I = 4mA. 62
Table 6.2: Modal content in y for I = 4mA. 62
Table 6.3: Modal content in x for I = 5mA. 64
Table 6.4: Modal content in y for I = 5mA. 65
Table 6.5: Modal content in x for I = 10mA. 66
Table 6.6: Modal content in y for I = 10mA. 67
Table 6.7: Modal content in x for I = 12mA. 68
Table 6.8: Modal content in y for I = 12mA. 69
Table 6.9: The percentage of each $G_n(x)$ to the beam's power. 71
Table 6.10: The percentage of each $G_m(y)$ to the beam's power. 71
Table 6.11: Modal content for I = 4mA at position z_1. 72
Table 6.12: The percentage of each $G_n(x)$ or $G_m(y)$ to the beam's power. 73
Table 7.1: The value of the M^2 factor is found from the variance curves in figure 7.6. 79
Table 7.2: The model of the beam at I = 2.5mA, as computed at z = 1 and 1.5mm. 81
Table 7.3: The model of the beam at I = 2.8mA, as computed at z = 1 and 1.5mm. 82
Table 7.4: The model of the beam at I = 3.5mA, as computed at z = 1 and 1.5mm. 83

1. Introduction

1.1 Motivation and objectives of thesis

Vertical cavity surface emitting lasers (VCSELs) are increasingly being used in optical systems such as free-space optical interconnects and fiber optic links [1]. The integration of such a device into a system requires knowledge of its operating characteristics. One of the most important characteristics is the transverse modal content of the intensity profile. The modal content of the beam will determine the size and shape of the beam and how it is modified by an optical system. The ability to predict power distribution at any point in an optical system will aid in the design of the system and allow for the system's performance to be predicted.

It has been demonstrated that the intensity profile of a VCSEL can be modeled using Hermite-Gauss (HG) or Laguerre-Gauss (LG) modes [2,3,4,5,6,7]. The choice of HG or LG functions to represent the modes will depend on the device used. This project used VCSELs whose emissions were best characterized by Hermite-Gauss functions at certain currents. The principle objective of this thesis is to obtain a mathematical representation of the VCSEL's output for a range of currents using the method for modal extraction developed by Gori et al. [8,9]. To the knowledge of the author of this thesis, the Gori et al. method has not been used by other researchers to extract the modal content from the experimentally measured intensity profile of a VCSEL. Where possible, the objective is to extract the modal content from the measured intensity profile. It will be demonstrated that in cases were the VCSEL's emission is not sufficiently Hermite-Gauss, and thus can not be accurately represented by HG functions alone, a partial model of the beam can be obtained.

The measurement of the intensity profiles required the choice of a measurement setup capable sampling data with sufficient resolution and accuracy to allow numerical representation of the beam. This project used two different experimental setups to measure intensity profiles. They will be described along with the data that was measured. The first setup consisted of a scanning near-field optical microscope (SNOM) which was used to sample the beam near the surface of the VCSEL. The second setup used a two-lens imaging system and intensity sampling equipment to acquire the intensity profiles. The purpose of using two setups to conduct similar experiments was to compare the quality data that was acquired by the two different methods. The quality of the data is implied by the ability of the modeling process to produce accurate models. The results obtained using the two setups were analyzed using the Gori et al. method.

1.2 Thesis organization

This thesis is structured as follows. A significant amount of information has been published on VCSELs and scanning near-field optical microscopy (SNOM). Chapter 2 presents a literature review on these two subjects. Chapter 3 presents the Hermite-Gauss family of functions which constitute the basis for the description of the modes of the VCSELs used in this project. Chapter 4 discusses the Gori et al. method. Three implementations of this method will be presented. Each method will provide a different model of the VCSEL output from which information can be obtained. These methods are applied to an ideal representation of a Hermite-Gauss beam in order to test the performance of the implementations of the Gori et al. method that are used in this project. Chapter 5 details the SNOM setup that was used to acquire intensity profiles. The data obtained is analyzed in Chapter 6. Partial models, which had a strong agreement with the VCSEL output, were found for several currents, and the modal content of the beam was calculated and is presented for one current. Chapter 7 describes the experimental setup consisting of a two-lens system and beam sampling equipment to obtain data which is then analyzed with Gori et al.'s method. Chapter 8 presents the conclusions reached from the work done and suggests future work.

1.3 References

[1] J. Martin-Regalado, S. Balle., M. San Miguel, A, Valle, L. Pesquera, "Polarization and transverse-mode selection in quantum-well vertical-cavity surface-emitting lasers: index- and gain-guided devices", Quantum Semiclass. Opt., Vol. 9, No. 5, October 1997, pp. 713-736.

[2] C. Degen, I. Fischer, W. Elsaber., "Transverse modes in oxide confined VCSELs: Influence of pump profile, spatial hole burning, and thermal effects", Optics Express, Vol. 5, No. 3, August 1999, pp. 38-47.

[3] O. Buccafusca, J.L.A Chilla, J.J. Rocca, P. Brusenbach, J. Martin-Regalado, "Transient Response of Vertical-Cavity Surface-Emitting Lasers with Different Active-Region Diameters", IEEE Journal of Quantum Electronics, Vol. 35, No. 4, 1999, pp. 608-615.

[4] C.J. Chang-Haisnain, M. Orenstein, A. Von Lehmen, L.T. Florez, J.P. Harbison, N.G. Stoffel, "Transverse mode characteristics of vertical cavity surface-emitting lasers", Appl. Phys. Lett., Vol. 57, No. 3, 1990, pp. 218-220.

[5] G.C. Wilson, D.M. Kuchta, J.D. Walker, J.S. Smith, "Spatial hole burning and self-focusing in vertical-cavity surface-emitting laser diodes", Appl. Phys. Lett. Vol.64, No. 5, 1994, pp. 542-544.

[6] C. Degen, B. Krauskopf, G. Jennemann, I. Fischer., W. Elsaber, "Polarization selective symmetry breaking in the near-fields of vertical cavity surface emitting lasers", J. Opt. B: Quantum Semiclass. Opt. Vol. 2, No. 4, 2000, pp. 517-525.

[7] T. Ackemann, et al., "Spatial mode structure of bottom-emitting broad-area vertical-cavity surface-emitting lasers", J. Opt. B: Quantum Semiclass. Opt., Vol. 2, No. 3 , 2000, pp. 406-412.

[8] F. Gori, M. Santarsiero, "Intensity-based modal analysis of partially coherent beams with Hermite-Gaussian modes", Optics Letters, Vol. 23, No. 13, July 1998, pp. 989-991.

[9] M. Santarsiero, F. Gori, R. Borghi, G. Guattari, "Evaluation of the modal structure of light beams composed of incoherent mixtures of Hermite-Gaussian modes", Applied Optics, Vol. 38, No. 25, September 1999, pp. 5272-5281.

2. Literature Review

2.1 Introduction

The information presented in this chapter is from published sources. Its purpose is to provide an understanding of vertical cavity surface emitting lasers (VCSELs) and scanning near-field optical microscopy (SNOM).

VCSELs can be used in many devices such as optical fiber communications, free-space communications, optical information storage and laser printers [1]. In order to determine how to model the modal content of a vertical cavity surface emitting laser (VCSEL) it is necessary to understand their principle characteristics. This includes their structure, behaviour under various operating conditions and the typical form of their output. Section 2.2.1 discusses the structure of VCSELs and the resulting advantages. Section 2.2.2 discuses the modal properties exhibited by typical VCSELs.

There has been significant work done to evaluate the modal content of VCSELs outputs. One such method involves the use of scanning near-field microscopy (SNOM) [2,3,4]. An introduction to SNOM is presented in section 2.2.

2.2 Vertical cavity surface emitting lasers (VCSELs)

2.2.1 VCSEL structure and advantages

VCSELs are small semiconductor lasers whose cavities are on the order of 1 um in length [5]. The cavity length determines the operating wavelength and the shape of the cavity can be rectangular or cylindrical. There are index-guided and gain-guided VCSELs [5]. The VCSELs used in this project were gain guided, thus the information presented in this chapter will focus on gain-guided VCSELs. A gain guided VCSEL uses proton implantation to confine the charge carriers to the laser cavity [3]. The picture below (figure 2.1) is of a proton-implanted device [6]. It is fabricated by sandwiching layers of Indium Gallium Arsenide and A luminum Gallium Arsenide, the combination of which will serve as a laser cavity, between p-doped and n-doped Bragg reflectors. The VCSEL is fabricated on a GaAs substrate that will serve as the n contact and a metal p contact is placed on the surface of the p-type Bragg reflector. The light can be coupled out of the p-type (top-emitter) or n-type (bottom emitter) reflector. The VCSELs used in this project are top-emitters. However, it has been observed that a bottom emitting VCSEL has better current and carrier distribution that a top emitting VCSEL [7]. This is due to the fact that in a top emitter, the contact pad which delivers the current to the p-mirror must have an aperture to allow the output light to escape, thus the current is not injected uniformly into the VCSEL [7]. Typical values for the reflectivity of the two Bragg reflectors are $R_1 >$ 0.9998 R2 > 0.992, and the light is coupled out of R_2 [7]. An antireflection coating is placed on the outside of the output mirror to prevent undesired back-reflections [7]. The structure of a VCSEL's cavity resembles the theoretical model of the spatial structure of broad area lasers [7].

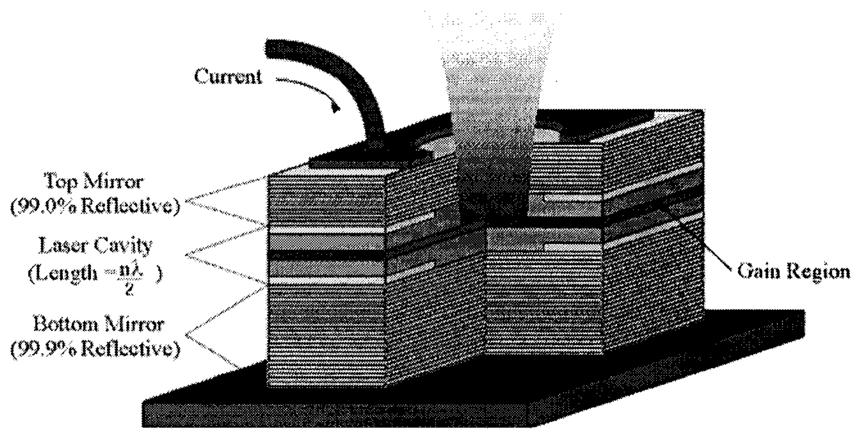

Figure 2.1: The structure of a VCSEL.

The structure of VCSELs gives them many advantages over other types of lasers. They have low threshold currents, are capable of high-speed modulation, and emit an astigmatism free beam [1,8]. Their vertical structure makes it possible to fabricate 2-D arrays on a single wafer. The individual devices in a VCSEL array can be tested without cutting out all the devices as must be done for edge emitters because the contacts for the current are on the top and bottom of the device and can be readily accessed [7]. The short cavity results in a single longitudinal mode [1]. The output beam will be circular if the cavity is uniform and symmetric. VCSELs have a low divergence and improved coupling to optical fibers over other lasers [3]. However, high temperatures will cause severe degradation in the VCSELs performance [3]. As the temperature increases the threshold current and wavelength increases [7]. The performance of a VCSEL will also deteriorate even if there is only small anisotropy in the VCSEL structure, due to the small size of the device [8].

2.2.2 Longitudinal and transverse modes of a VCSEL

The output of a VCSEL consists of longitudinal and transverse modes. Longitudinal modes refer to the number of distinct wavelengths that are emitted by the VCSEL. The spectrum of a typical VCSEL output has several wavelength peaks. Although the transverse modes occur at slightly different wavelengths, because the spectral width of the output is less than 1nm, the output is said to be single mode in the longitudinal sense. The VCSELs used in this project have a wavelength equal to 850nm. Transverse modes refer to the distribution of the electric field in space. In the case of lasers with uniform cavities, they can be represented using Hermite-Gauss (HG) or Laguerre-Gauss (LG) functions for the cases where the cavity shape is rectangular or cylindrical respectively. However, it has been observed that if the cavity of a cylindrical VCSEL is anisotropic HG modes can occur [8]. The mathematical representation of HG and LG modes will be discussed in further detail in Chapter 3. The existence of HG or LG modes in a VCSEL output is a result of waveguiding in the laser cavity [9]. The waveguiding is a combination of index guiding, gain guiding, thermal guiding and carrier-induced antiguiding [9].

As the current is increased the number of transverse modes increases. The spectrum also shifts to longer wavelengths, corresponding to lower energies, due to heating of the laser [4]. The transverse modes occur at slightly different wavelengths. The wavelength separation of the modes will be inversely proportional to the active area of the VCSEL [10]. One method of evaluating modal composition utilizes the small difference in wavelength between the transverse modes. Using a spectrum analyzer, the different wavelengths can be isolated and the modes measured separately [11]. Higher order modes occur at longer wavelengths than the fundamental mode [1]. The number of transverse modes may be on the order of 10^2 [11]. Although the total power emitted by a VCSEL will increase linearly with current, the power content of the individual modes does not. Over certain ranges of current, the amount of power associated with a mode may decrease slightly even though the current has increased [2]. The modes compete for the available power with higher order modes generally being favoured at larger current [8]. The modal content at a particular current is the combination that uses the available gain most efficiently [8].

The modal behavior of the VCSEL will also depend on the size of the laser cavity. Larger device are generally capable of delivering more power, however their outputs will also have a larger number of modes than for smaller devices [8]. The beam waist of the fundamental mode will increase with a square root dependence as the active area is increased [12]. This results in more available gain media in the outer periphery of the cavity to support multimode oscillation [10]. Thus larger VCSELs can support more modes. At low currents the central region of the cavity will output stimulated emissions. The outer area will emit spontaneous emissions which add noise to the signal. As the current is increased a larger portion of the cavity emits stimulated emissions and the noise level in the signal will decrease [10]. Thus, when larger VCSEL are in use it is necessary to drive them at a current large enough to emit several modes such that the signal is not noisy. Larger VCSELs exhibit less competition between modes due to the larger amount of available gain media and are thus less prone to mode hopping than smaller VCSELs [10].

The modal content of the beam is also influenced by the carrier density as a function of the transverse dimensions [1]. The carrier distribution is in turn determined by the carrier diffusion, the leakage current and spatial hole burning [1]. Spatial hole burning is less prominent the smaller the pump region [1]. The distribution of the charge carriers is determined in part by spatial hole burning [13,14,15]. The 'donut' mode, a commonly observed output of VCSELs, is a result of spatial hole burning [16].

2.3 Scanning near-field optical microscopy (SNOM)

SNOM, as the name implies, is the imaging of an object via the collection of light in the near-field. The near-field is the region of space within $\lambda/2\pi$ of the object, where λ is the wavelength of the light used. A small optical probe is scanned over the object under study and the image of the object is obtained by a photo-detector. The probe's aperture will range from 20nm to 500nm [17]. The resolution of the image is determined by the size of the aperture in the optical probe and thus can be close to the resolution of the electron microscope [18]. The best type of probe is a tapered single mode optical fiber [17]. This type of probe can be constructed by etching the fiber in acid to produce a sharp tip. The fiber is aluminum coated to ensure that only light sampled by the fiber tip is coupled into the fiber [17]. The collected data is independent of wavelength when the aperture is positioned in the near-field of the object under study. The resolution will depend solely on the size of the aperture. This can produce images with a resolution of approximately 50nm when the probe is about 20nm from the surface [18]. By comparison a lens has a resolution limited to $1.22 * f * \lambda / D$, where f and D are the focal length and the diameter of the lens respectively [19]. Thus SNOM, which can operate beyond the diffraction limit, has a much better resolution than a lens based system because it can resolve smaller details, which can be much smaller than the wavelength of the light being collected [17].

There are three methods of performing SNOM, illumination, collection and combined illumination/collection [20]. The illumination method uses the optical probe to illuminate a sample and the detector collects either the reflected light or the light that is transmitted through the sample. When used in the illumination mode, as an alternative to the electron microscope, the advantages are the use of non-destructive radiation, i.e. visible light, and it can operate in air [18]. The collection method uses the optical probe to collect light reflected off of the sample. SNOM can also be used in the collection mode to profile the outputs of light emitting samples such as laser diodes [2,3,4,21]. Betzig et al. performed the first experiments using the SNOM in the collection mode [18]. They used an aluminum coated pipette as the optical probe. The aperture was formed by pulling the pipette until it split in two [18]. The combined illumination/collection mode uses the optical probe to both illuminate the sample and collect the reflected light which is then transmitted to the detector.

It is desirable to incorporate into a SNOM setup a z-control mechanism to maintain a constant probe to object height. This will ensure that the image is not distorted and prevent the probe from striking the sample. Betzig et al. tested three different methods of controlling the separation of the optical probe and the test sample [18]. Tunneling feedback allowed the SNOM to monitor the probe distance during a scan but resulted in images of a poor quality in addition to being slow. The second method was contact mode tunneling under where the probe is moved toward the object until a tunneling current is measured. However, there is no method to maintain the probe to object separation once the scan is begun. The final method used by Betzig et al. was to perform a scan, observe the resolution and move the probe closer if a greater resolution was required. The last two methods require that the device under test is flat to avoid damage to the probe or the device. There are other possible methods of implementing feedback, such as oscillating the fiber tip at a frequency corresponding to the piezo voltage [22]. As the tip approaches the surface the change in the amplitude and phase of the oscillation can be measured and used as a feedback mechanism to control the height [22].

2.4 Conclusion

The objective of this thesis is to model the experimentally acquired output of a VCSEL. The information presented in section 2.2.1 and 2.2.2 is required to understand the behaviour of the modal content of the emissions of the VCSEL under test conditions. The properties of SNOM make it an ideal method of obtaining intensity profiles of a VCSEL in the near field. The optical probe used in SNOM is small enough and possesses sufficient resolution to sample the beam within less than a wavelength of the location of the beam waist [23]. The impulse response of a SNOM is much narrower when compared to that of other optical systems, which will reduce distortion of the data when compared to other measurement systems [17].

2.5 References

[1] J. Martin-Regalado, S. Balle., M. San Miguel, A, Valle, L. Pesquera, "Polarization and transverse-mode selection in quantum-well vertical-cavity surface-emitting lasers: index- and gain-guided devices", Quantum Semiclass. Opt., Vol. 9, No. 5, October 1997, pp. 713-736.

[2] K.J. Knopp, D.H. Christensen, G. Vander Rhodes, J.M. Pomeroy, B.B. Goldberg, M. Selim Unlu, "Spatio-Spectral Mapping of Multimode Vertical Cavity Surface Emitting Lasers", Journal of Lightwave Technology, Vol. 17, No. 8, 1999, pp. 1429-1435.

[3] J.A. DeAro, K.D. Weston, R.W. Herrick, P.M. Petroff, S.K. Buratto, "Near-field scanning optical microscopy of cleaved vertical-cavity surface-emitting lasers", Semiconductor Science and Technology vol. 13, no 12, 1998, pp. 1364-1367.

[4] I. Horsch, R. Kusche, O. Marti, B. Weigl, K.J. Ebeling, "Spectrally resolved near-field mode imaging of vertical cavity semiconductor lasers", J. Appl. Phys., vol.79, no.8, pt.1, 1996, pp. 3831-3834.

[5] V.N. Morozov, J.A. Neff, H. Zhou, "Analysis of Vertical-Cavity Surface-Emitting Laser Multimode Behaviour", IEEE Journal of Quantum Electronics, Vol. 33, No. 6, June 1997, pp. 980-988.

[6] http://www.physics.montana.edu/optics/jlc/VCSEL.gif

[7] T. Ackemann, et al., "Spatial mode structure of bottom-emitting broad-area vertical-cavity surface-emitting lasers", J. Opt. B: Quantum Semiclass. Opt., Vol. 2, No. 3 , 2000, pp. 406-412.

[8] C. Degen, B. Krauskopf, G. Jennemann, I. Fischer., W. Elsaber, "Polarization selective symmetry breaking in the near-fields of vertical cavity surface emitting lasers", J. Opt. B: Quantum Semiclass. Opt. Vol. 2, No. 4, 2000, pp. 517-525.

[9] N.A. Loiko, I.V. Babushkin, "Competition of orthogonally polarized transverse Fourier modes in a VCSEL", J. Opt. B: Quantum Semiclass. Opt., Vol. 3, No. 2, April 2001, pp. S234-S243.

[10] O. Buccafusca, J.L.A Chilla, J.J. Rocca, P. Brusenbach, J. Martin-Regalado, "Transient Response of Vertical-Cavity Surface-Emitting Lasers with Different Active-Region Diameters", IEEE Journal of Quantum Electronics, Vol. 35, No. 4, 1999, pp. 608-615.

[11] F. Marin, G. Giacomelli, "Polarization and transverse mode dynamics of VCSELs", J. Opt. B: Quantum Semiclass. Opt., Vol. 1, No. 1, February 1999, pp. 128-132.

[12] D.I. Babic, R.J. Ram, J.E. Bowers, M.Tan, L. Yang, "Scaling laws for gain guided vertical cavity lasers with distributed Bragg reflectors", Appl. Phys. Lett., Vol. 64, No. 14, 1994, pp. 1762-1764.

[13] G. C. Wilson, D. M. Kuchta, J. D. Walker, J. S. Smith, "Spatial hole burning and self-focusing in vertical-cavity surface-emitting laser diodes", Appl. Phys. Lett., Vol. 64, No. 5, 1994, pp. 542-544.

[14] D. Vakhshoori, J.D. Wynn, G.J. Zydzik, R.E. Leibenguth, M.T. Asom, K. Kojima, R.A. Morgan , "Top-surface emitting lasers with 1.9 V threshold voltage and the effect of spatial hole burning on their transverse mode operation and efficiencies", Appl. Phys. Lett., Vol. 62, No. 13, 1993, pp. 1448-1450.

[15] A. Valle, J. Sarma, K.A. Shore, "Spatial holeburning effects on the dynamics of vertical cavity surface-emitting laser diodes", Quantum Electronics, IEEE Journal of , Vol. 31, No. 8 , August 1995, pp. 1423 –1431.

[16] J. Wilk, R.P. Sarzala, W. Nakwaski, "The spatial hole burning effect in gain-guided vertical-cavity surface-emitting lasers", J. Phys. D: Appl. Phys., Vol. 31, No. 4, February 1998, pp. L11-L15.

[17] E. Betzig, J.K. Trautman, T.D. Harris, J.S. Weiner, R.L.Kostelak, "Breaking the Diffraction Barrier: Optical Microscopy and a Nanometric Scale", Science Vol. 251, No. 5000, 1991, pp.1468-1470.

[18] E. Betzig, M Issacson, A. Lewis, "Collection Mode near-field scanning optical microscopy" , Appl. Phys. Lett., vol.51, no. 25, 1987, pp. 2088-2090.

[19] Eugene Hecht, *Optics*, Addison-Wesley, Don Mills, Ontario, 1998, pp. 464.

[20] D. Courjon, F. Baida, "Near Field Instrumentation", in *Photons and local probes*, O. Marti, R. Moller, Ed., NATO ASI Series: Applied Sciences, Boston, Massachusetts, 1995, pp. 55-77.

[21] W.D. Herzog, M.S. Unlu, B.B. Goldberg, G.H. Rhodes, "Beam divergence and waist measurements of laser diodes by near-field scanning optical microscopy", Appl. Phys. Lett., Vol.70, No. 6, 1997, pp.688-690.

[22] J. Barenz, O. Hollricher, O. Marti, "An easy-to-use non-optical shear-force distance control for near-field optical microscopes", Rev. Sci. Instrum., Vol.67, No. 5, 1996, pp. 1912-1915.

[23] E. Betzig, J.K. Trautman, "Near-field optics: microscopy, spectroscopy, and surface modification beyond the diffraction limit", Science, vol.257, no.5067, 1992, pp. 189-195.

3. Multi-transverse mode laser output characterization

3.1 Introduction

The widespread use of multi-transverse mode lasers has resulted in considerable study of their beam characteristics. The ability to model the power distribution at any point along the optical axis will allow a designer to optimize the performance of an optical system. It has been demonstrated that large uniform stable cavity lasers will emit transverse modes that are described by the Hermite-Gauss (HG) or the Laguerre-Gauss (LG) family of functions [1]. The intensity profile that can be measured will be a linear combination of the modes. It has further been demonstrated that these models can be applied to certain VCSELs despite the small size of the VCSEL cavity [2,3,4,5,6,7]. A beam that is composed solely of HG or LG modes will exhibit symmetry about the two transverse axes, denoted as x and y. The models will characterize both single and multi-transverse mode lasers.

This chapter is structured as follows. The Gaussian beam model is presented in section 3.2. This function is used to model the output of a laser emitting a single transverse mode. The Gaussian function also serves as the root function of the Hermite and Laguerre Gauss modes which are described in section 3.3. Section 3.4 defines the M^2 factor which describes beam quality and is related to the modal content of the beam.

3.2 Gaussian beam model

A multimode laser operating at a low driving current near its threshold current, may emit a beam that can be described by a Gaussian function [2]. As the current is increased the Gaussian mode may continue to contribute to the output. The Gaussian mode is also known by the designations HG_{00} and TEM_{00}. Consider a bias condition which results in a purely Gaussian output. The Gaussian mode can be used to model the propagation of a beam through an optical system as it is modified by optical components such as lenses. The equation representing the magnitude and phase of the electric field of a Gaussian beam is given by equation 3.1 [8]. It is not possible to experimentally measure the phase component of the beam, thus for the purpose of modeling the beam one will consider the intensity function. Generally, if the basis for the model is HG the intensity is described by a Gaussian in x, y, z, where x and y describe the transverse axes and z is the optical axis along which the beam will propagate (Eqn 3.2). Should the geometry of the laser cavity be cylindrical it is preferable to express the function in cylindrical coordinates (Eqn 3.3). Figure 3.1 is a plot of magnitude of the electric field versus radial distance from the optical axis.

$$\tilde{E}(x,y,z) = \sqrt{\frac{2P_0}{\pi}} \frac{\exp[-jkz + j\psi(z)]}{\omega(z)} \exp\left(\frac{-(x^2+y^2)}{\omega^2(z)} - jk\left(\frac{x^2+y^2}{2R(z)} \right) \right) \quad \text{(Eqn 3.1)}$$

$$I(x,y,z) = \left| \tilde{E}(x,y,z) \right|^2 = \frac{2P_0}{\pi\omega^2(z)} \exp\left(\frac{-2(x^2+y^2)}{\omega^2(z)} \right) \quad \text{(Eqn 3.2)}$$

$$I(r,z) = \frac{2P_0}{\pi\omega^2(z)} \exp\left(\frac{-2r^2}{\omega^2(z)} \right) \quad \text{(Eqn 3.3)}$$

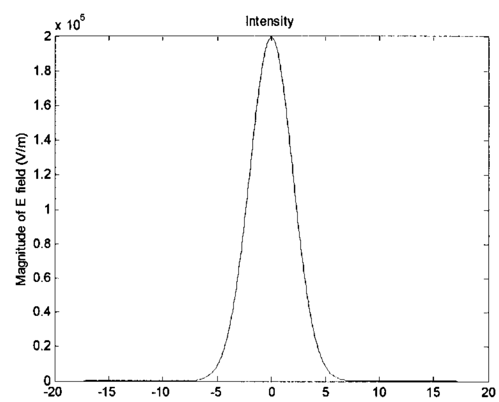

Figure 3.1: Plot of the intensity function vs. radial distance from the optical axis. The value of the beam waist radius is $\omega_0 = 4\mu m$.

The P_0 term in the equations represents the total power contained by the beam. The mathematical representation of a Gaussian beam is of infinite extent. In order to define a finite definition for the beam radius the distribution of the power is examined. The power content of the beam within a circular area with radius R can be evaluated at a position $z = z_1$ by integrating the intensity function (Eqn 3.4).

$$P(r,z) = P_0 \int_0^{2\pi} \int_0^R \frac{2}{\pi\omega^2(z)} \exp\left(\frac{-2r^2}{\omega^2(z)}\right) r\,dr\,d\theta = P_0\left[1-\exp\left(\frac{-2R^2}{\omega^2(z)}\right)\right] \qquad \text{(Eqn 3.4)}$$

Substituting $R = \omega(z)$ into equation 3.4 we obtain $P(r,z) = 0.865*P_0$. Thus 86.5% of the power is contained within a radius equal to $\omega(z)$. The parameter $\omega(z)$, known as the beam radius, also corresponds to the radial distance from the optical axis where the intensity has dropped to $1/e^2$ its maximum value. At points were $\omega(z = 0) = \omega_0$, this parameter is also referred to as the beam waist radius or simply the beam waist and corresponds to the minimum radial size of the laser spot. Since a theoretical Gaussian curve is of infinite extent, the beam radius quantifies the radial extent of the beam for practical purposes. This aids in the design of optical systems using single-mode lasers. The size of optical components such as lenses, with respect to the size of the beam waist, will affect the performance of an optical system. Choosing components that are too small will result in power loss as well as distortion of the beam. The amount of captured power that is acceptable will vary depending on the application. A useful property of the Gaussian profile is that 99% of the power is contained within $1.5*\omega(z)$. Another useful term, predominantly used for multimode beams but also applies to single mode beams, is the mode-field diameter which is simply the diameter of the beam. In the case of the Gaussian distribution this is equal to $2*\omega(z)$.

The behavior of the Gaussian curve as it propagates through an optical system is well understood. Equation 3.5 gives the expression for the evolution of the profile as it propagates in free space [9]. As can be seen by the equation, $\omega(z)$ increases in size as the beam propagates away from the optical axis. The term z_R (Eqn 3.6), known as the Rayleigh range, designates the distance from the beam waist to where the beam is equal to $\sqrt{2}*\omega_0$ [9]. θ_0 is the half-width divergence angle (Eqn 3.7) [9]. It gives an approximate measure of the divergence of the beam in the far field.

$$\omega(z) = \omega_0 \left[1 + \left(\frac{z}{z_0} \right)^2 \right]^{\frac{1}{2}} \qquad \text{(Eqn 3.5)}$$

$$z_R = \frac{\pi \omega_0^2}{\lambda} \qquad \text{(Eqn 3.6)}$$

$$\theta_0 = \frac{\lambda}{\pi \omega_0} \qquad \text{(Eqn 3.7)}$$

In addition a Gaussian beam which is modified by a lens remains Gaussian. The size and location of the new waist can be found by using equations 3.8 and 3.9 respectively [10]. In the equations, ω_1 and ω_2 are the initial and modified waists, z_1 and z_2 the distances from the waists to the closest focal points, f is the focal length of the lens and z_{R1} is the Rayleigh range of the incident beam. Thus it is possible to model the beam throughout the optical system.

$$\omega_2 = \frac{f \omega_1}{\sqrt{z_1^2 + z_{R1}^2}} \qquad \text{(Eqn 3.8)}$$

$$z_2 = \frac{-x_1 f^2}{z_1^2 + z_{R1}^2} \qquad \text{(Eqn 3.9)}$$

For many types of lasers, the Gaussian model is not sufficient due to the presence of higher order modes described by the Hermite-Gauss and Laguerre-Gauss families of functions. As is implied by the terms Hermite-Gauss and Laguerre-Gauss, the Gaussian function is the foundation upon which the HG and LG functions are constructed.

3.3 Hermite-Gauss and Laguerre-Gauss functions

In general, because a multimode VCSEL will only emit a pure Gaussian output at low currents insufficient power is released for most applications. Thus it is necessary to increase the driving currents. This causes higher order modes to be emitted. These modes are described by the higher order HG or LG functions. For simplicity, the properties of the HG functions can be examined for one transverse dimension and the results generalized to 2-D. The form of the HG functions is given by equation 3.10 [11,12].

$$G_n(x) = \left(\frac{2}{\pi\omega_0^2}\right)^{\frac{1}{4}} * \frac{1}{\sqrt{2^n n!}} * H_n\left(\frac{x\sqrt{2}}{\omega_0}\right) * \exp\left(\frac{-x^2}{\omega_0^2}\right) \qquad \text{(Eqn 3.10)}$$

The term H_n represents the Hermite polynomials which are a solution to the differential equation given by equation 3.11 [13].

$$H_n(u) = (-1)^n e^{u^2} \frac{d^n}{dx^n}(e^{-u^2}) \qquad \text{(Eqn 3.11)}$$

Examining the inner product of two HG functions, it is observed that the Hermite-Gauss functions form an ortho-normal basis of functions (Eqn 3.12).

$$\int_{-\infty}^{\infty} G_n(x)G_m(x)dx = \begin{cases} 0, n \neq m \\ 1, n = m \end{cases} \qquad \text{(Eqn 3.12)}$$

The Hermite-Gauss functions will describe the modes of a uniform rectangular cavity laser. However, if the cavity is cylindrical Laguerre-Gauss functions are used as the basis. The Laguerre-Gauss equations can be obtained replacing H_n by L_n in equation 3.11. The Laguerre-Gauss equations are a solution to the differential equation given by equation 3.13 [12].

$$L_n(u) = e^u \frac{d^n}{dx^n}(u^n e^{-u}) \qquad \text{(Eqn 3.13)}$$

Table 3.1 lists the first six Hermite and Laguerre polynomials.

n	$H_n(u)$	$L_n(u)$
0	1	1
1	$2u$	$-u+1$
2	$4u^2 - 2$	$u^2 - 4u + 2$
3	$8u^3 - 12u$	$-u^3 + 9u^2 - 18u + 6$
4	$16u^4 - 48u^2 + 12$	$u^4 - 16u^3 + 72u^2 - 96u + 24$
5	$32u^5 - 160u^3 - 120u$	$-u^5 + 25u^4 - 200u^3 + 600u^2 - 600u + 120$

Table 3.1: The first six Hermite and Laguerre polynomials.

The VCSELs that are examined in this thesis have rectangular cavities and thus will be modeled using HG functions. Thus the focus of the remaining chapters will be on HG modes. Figure 3.2 contains a plot of the first three HG functions. Figure 3.3 displays the result of applying an FFT to these functions. The Fourier transform of a HG function is a new HG function of the same order. Since beam modification by a lens can be seen as a Fourier transform this implies that a HG beam remains HG when propagating through a lens relay system although the beam waist parameter in the equation will be modified by equation 3.8 and its new position given by equation 3.9. Applying a Fourier transform to the square of a HG function will result in a LG function of the same order (figure 3.4). This result will have implications in the extraction of the modal content of a laser and will be examined further in Chapter 4.

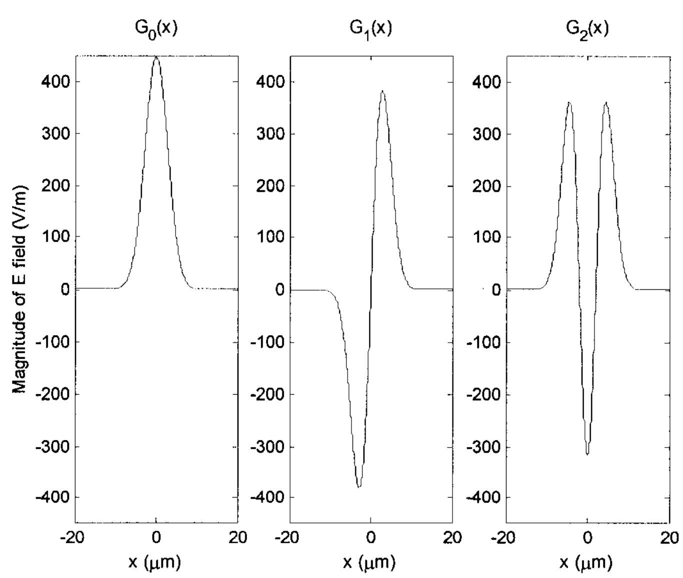

Figure 3.2: Plots of the first three Hermite-Gauss functions (G_0,G_1, G_2). The value of the beam waist radius is $\omega_0 = 4\mu m$.

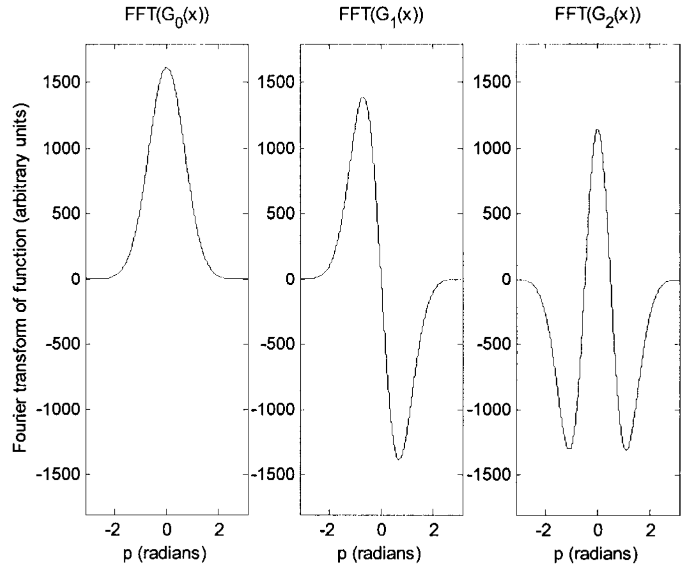

Figure 3.3: Plots of the FFTs of the first three Hermite-Gauss functions (G_0,G_1, G_2). The results are Hermite-Gauss functions of the same order as the initial functions.

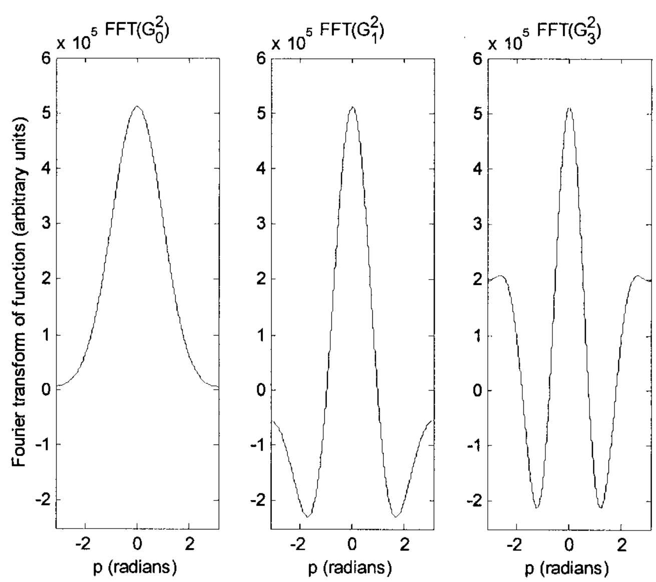

Figure 3.4: Plots of the FFTs of the squares of the first three Hermite-Gauss functions (G_0^2,G_1^2, G_2^2). The results are Laguerre-Gauss functions of the same order as the initial functions.

HG functions in two transverse dimensions are obtained by multiplying $G_n(x)$ and $G_m(y)$, where n and m are independent indices spanning the ranges n = 0,1…N and m = 0,1,…M. Each combination of n and m corresponds to a possible transverse mode (Eqn 3.14).

$$u_{nm}(x,y) = G_n(x)G_m(y) \qquad \text{(Eqn 3.14)}$$

The functions are orthonormal functions. Thus each mode is independent of the others and can be scaled to represent the power it contains. The $u_{nm}(x,y)$ functions remain HG as they propagate through free space or lenses. The equation representing a mode can be found at any point z along the optical axis by replacing ω_0 with $\omega(z)$, which is evaluated using the Gaussian beam equation (Eqn 3.5). The intensity of the beam is found by summing the contributions of each mode (Eqn 3.15) [14]. The total power carried by a beam can then be found by integrating the intensity profile over area for a fixed value of z. The coefficient c_{nm} is the power content of each mode.

$$I(x,y) = \sum_{m=0}^{\infty}\sum_{n=0}^{\infty} c_{nm}\left|u_{nm}(x,y)\right|^2 \qquad \text{(Eqn 3.15)}$$

Assuming that ω_0 is known through knowledge of the laser cavity or it can be evaluated, then equations representing all possible modes $u_{nm}(x,y)$ are known. Given that intensity profile is composed of HG modes, a method of evaluating the modal content has been developed by Gori et al. [11]. This is done by extracting the c_{nm}'s and will be discussed in Chapter 4.

3.4 M^2 factor

The HG and LG models offer detailed descriptions of a laser's output. However, extracting the HG modes is complex. For applications where detail is not required there exists a commonly used model known as the M^2 factor. The M^2 factor describes a beam's quality. Its purpose is to compare beams to a single mode beam and allow the use of the properties and equations which have been developed for Gaussian beams. The M^2 factor defines the Gaussian beam to have the highest quality with $M^2 = 1$. Multimode beams will have a rating of $M^2 > 1$, the closer the beams properties are to a Gaussian beam to the closer the beam's rating is to 1. Defined as such, the M^2 factor is an inverse quality factor.

There are several methods which can be used to define the M^2 factor. The first definition is given by equation 3.16 [1].

$$M^2 = \left(\frac{\omega_{0M}}{\omega_0} \right)^2 \qquad \text{(Eqn 3.16)}$$

It relates the beam waist of the entire multimode beam, ω_{0M}, to the waist of the lowest order mode for that laser, i.e. the HG_{00} mode with beam waist ω_0. The M^2 factor need not be the same for the x-axis and the y-axis. It should be noted that even in the case where a multimode laser beam does not contain a HG_{00} component this definition still has value because as noted in section 3.3, the shape of the higher order modes is characterized using the parameter ω_0. It also suggests a method for modifying the Gaussian beam equations by substituting ω_0^2 by ω_{0M}^2/M^2 (Eqn 3.17) [15].

$$\omega_M(z) = \omega_{0M} \left[1 + \left(\frac{M^2 z \lambda}{\pi \omega_{0M}^2} \right)^2 \right]^{\frac{1}{2}} \qquad \text{(Eqn 3.17)}$$

This definition implies that a multimode beam will be larger than the corresponding single mode beam. In addition the multimode beam will diverge more rapidly than the single mode beam (Eqn 3.18) [15]. These properties must be taken into account when sizing optical components for a multimode system.

$$\Phi_0 = M\theta_0 = \frac{M^2 \lambda}{\pi \omega_{0M}} \qquad \text{(Eqn 3.18)}$$

A second definition, given by equation 3.19 indicates that the M^2 factor is dependent upon the power distribution among the modes in the laser [1]. Since the M^2 factor is related to the modal content it will not be a constant value for a given laser and thus must be evaluated for all currents of interest. This relationship also indicates that the same M^2 factor can be obtained for several modal combinations. For example, a beam that is 60% HG_{00}, 30% HG_{10} and 10% HG_{20} and another beam that is 50% HG_{00} and 50% HG_{10} will both have $M^2_x = 1.4$ for the x-axis and $M^2_y = 1$ for the y-axis. However, these two beams do not have similar shapes. Thus the M^2 factor indicates the presence of multimode components, but it does not provide a clear indication of which higher order modes are present, nor does it indicate what their power contributions are.

$$M_x^2 = \sum_{n,m}\left[\left(\frac{c_{nm}}{\sum_{n,m} c_{nm}}\right) * (2n+1)\right] \qquad \text{(Eqn 3.19)}$$

The M^2 factor is primarily used to determine the spot size as a laser beam propagates through an optical system when a Gaussian model is inapplicable. Before using the Gaussian model it is necessary to verify if the beam is indeed purely Gaussian. This can be accomplished by visual inspection when a beam is clearly not Gaussian in shape due to the presence of high order modes. However, a beam that appears to be nearly Gaussian is not necessarily so because certain combinations of high order modes can have a shape which is very close to Gaussian [16]. Under such circumstances, using a Gaussian model will results in incorrect calculated spot sizes in the optical system resulting in unexpected system behaviour. The M^2 factor can be used to verify if a beam which appears to be Gaussian is in fact Gaussian.

The advantages of the M^2 factor are that it enables the use of the properties of Gaussian beams and it is easy to measure. It provides an approximation of the area within which the power is contained. However, it gives no indication of the spatial distribution of that power within that area. It can be used as a simple alternative to the determination of the modal content, or in the event where the modal content is known, the M^2 factor can be calculated from the modal weights. Although the M^2 factor is not sufficient to adequately represent a complex multimode beam, it can be used in conjunction with knowledge of the modal content to evaluate a VCSEL beam's behaviour in an optical system.

3.5 Conclusion

This chapter presented the commonly used models for laser outputs. The properties of the Gaussian beam were examined. The discussion was then extended to the Hermite-Gauss family of functions which describe the modes in a laser whose cavity is rectangular and Laguerre-Gauss family of functions used for cylindrical cavities. It was shown how an intensity profile is described mathematically using the HG functions. The properties of the HG functions in an optical system were also presented. In addition, the M^2 factor, which is a simple indicator of spot size and modal content was discussed. This information is used in the next chapter to obtain numerical models of the shape of a VCSEL's output.

3.6 References

[1] A. E. Siegman, S.W. Townsend, "Output Beam Propagation and Beam Quality from a Multimode Stable-Cavity Laser", IEEE Journal of Quantum Electronics, Vol. 29, No. 4, April 1993, pp. 1212-1217.

[2] C. Degen, I. Fischer, W. Elsaber., "Transverse modes in oxide confined VCSELs: Influence of pump profile, spatial hole burning, and thermal effects", Optics Express, Vol. 5, No. 3, August 1999, pp. 38-47.

[3] O. Buccafusca, J.L.A Chilla, J.J. Rocca, P. Brusenbach, J. Martin-Regalado, "Transient Response of Vertical-Cavity Surface-Emitting Lasers with Different Active-Region Diameters", IEEE Journal of Quantum Electronics, Vol. 35, No. 4, 1999, pp. 608-615.

[4] C.J. Chang-Haisnain, M. Orenstein, A. Von Lehmen, L.T. Florez, J.P. Harbison, N.G. Stoffel, "Transverse mode characteristics of vertical cavity surface-emitting lasers", Appl. Phys. Lett., Vol. 57, No. 3, 1990, pp. 218-220.

[5] G.C. Wilson, D.M. Kuchta, J.D. Walker, J.S. Smith, "Spatial hole burning and self-focusing in vertical-cavity surface-emitting laser diodes", Appl. Phys. Lett. Vol.64, No. 5, 1994, pp. 542-544.

[6] C. Degen, B. Krauskopf, G. Jennemann, I. Fischer., W. Elsaber, "Polarization selective symmetry breaking in the near-fields of vertical cavity surface emitting lasers", J. Opt. B: Quantum Semiclass. Opt. Vol. 2, No. 4, 2000, pp. 517-525.

[7] T. Ackemann, et al., "Spatial mode structure of bottom-emitting broad-area vertical-cavity surface-emitting lasers", J. Opt. B: Quantum Semiclass. Opt., Vol. 2, No. 3 , 2000, pp. 406-412.

[8] A.E. Siegman, *Lasers*, University Science Books, Mill Valley, California, 1986, pp. 664.

[9] B.E.A. Saleh, M.C. Teich, *Fundamentals of Photonics*, John Wiley & Sons, Toronto, 1991, pp. 80-107.

[10] A. G. Kirk, private communication, January 2002.

[11] F. Gori, M. Santarsiero, "Intensity-based modal analysis of partially coherent beams with Hermite-Gaussian modes", Optics Letters, Vol. 23, No. 13, July 1998, pp. 989-991.

[12] M. Santarsiero, F. Gori, R. Borghi, G. Guattari, "Evaluation of the modal structure of light beams composed of incoherent mixtures of Hermite-Gaussian modes", Applied Optics, Vol. 38, No. 25, September 1999, pp. 5272-5281.

[13] M.R. Spiegel, J.M. Liu, "Schaum's Mathematical Handbook of Formula's and Tables", 2nd ed., McGraw-Hill, New York, New York, 1998, pp. 167-172.

[14] Xin Xue, H. Wei, A.G. Kirk, "Intensity based modal decomposition of optical beams in terms of Hermite-Gauss functions", J. Opt. Soc. Am. A, Vol. 17, No. 6, 2000, pp. 1086-1091.

[15] T.F. Johnson, J.r., "M^2 concept characterizes beam quality", a reprint from Laser Focus World, May 1990.

[16] C. Roundy, "Beam-Profile Analysis: Propagation factor quantifies laser beam performance", Laser Focus World, Vol. 35, No. 12, December 1999, 119-22.

4. Theoretical basis for the extraction of HG modes

4.1 Introduction

In Chapter 3, the mathematical representation of the modes that constitute a Hermite-Gauss beam was presented. To obtain this model of the output of a laser, in this case a VCSEL, it is necessary to determine the modal content of the beam. A method for evaluating the modes has been developed by Gori et al. [1,2]. This method will be used in Chapters 6 and 7 to model the outputs of actual VCSELs. Before proceeding with experimental results, it is necessary to examine the theoretical method and implement it in a form which can be applied to experimentally acquired data. In their paper, Gori et al. developed their method for an intensity profile represented as a one-dimensional function of the x transverse dimension. In practice, the measurement of a real laser beam requires that the beam be impulse point sampled over an x-y plane at a fixed z-position along the optical axis, thus resulting in a discrete-space representation of the beam. Thus, the modeling process must be implemented in discrete-space. Conversion from an ideal continuous-space domain to a discrete domain implies that the modeling process will have an associated error. It is necessary to test the behaviour of the modeling process in order to determine the requirements on the data sampling procedure in order to obtain the most accurate results.

The purpose of this chapter is to apply the Gori et al. method to an idealized representation of an experimentally sampled beam in order to test the accuracy of the modeling process. The discrete profile used represents an idealized version of a VCSEL beam that could be sampled in a laboratory, because it is noise free and is composed solely of Hermite-Gauss modes without any distortions. This chapter is structured as follows. The continuous domain method developed by Gori et al. is presented. This method is then implemented using three discrete domain techniques. Each of these techniques will construct a different model of the beam under study. The information that these models reveal and their performance as well as limitations will be examined as the models are applied to a beam propagating in free space. The first two techniques operate on a one transverse dimension representation of the theoretical beam. The third method, operates on the two transverse dimension beam representation and will provide a complete model of the beam by evaluating the modal constants. Having examined the three techniques, this information will be used to determine requirements on the sampling process that will be used to experimentally acquire the VCSEL output in Chapters 6 and 7. The penultimate section of this chapter discusses the determination the beam waist radius ω_0 from the intensity profile. The final section discusses the application of the M^2 factor to the beam under study.

4.2 The method presented by Gori et al.

As described in Chapter 3, the intensity profile of a beam composed of HG modes has the form given by equation 3.14. Gori et al. have demonstrated that it is possible to determine the modal weights from a single intensity profile [1,2]. In developing their method, Gori et al. chose to examine only one transverse axis at a z-position corresponding to the beam waist. Thus equation 3.14 can be simplified to equation 4.1. The method will be generalized to two dimensions in a following section.

$$I(x) = \sum_{n=0}^{\infty} c_n \left| G_n(x) \right|^2 \qquad \text{(Eqn 4.1)}$$

$G_n(x)$ was defined by equation 3.10. Examining equation 3.10, it is observed that the method is applied to the beam at a z-position corresponding to the beam waist. It can be applied at other points along the optical axis by replacing ω_0 by $\omega(z)$ which can be evaluated for any z using equation 3.5 from chapter 3. The assumption required is that ω_0 can be determined. Gori et al. suggest that ω_0 can be determined through knowledge of the VCSEL cavity [1]. Alternatively, ω_0 can be determined experimentally as will be discussed in section 4.9.

Equation 4.1 is clearly a linear combination of the $G_n^2(x)$ functions. It is known that a function, which is obtained from a linear combination of ortho-normal functions, can be decomposed into its basis functions by calculating the inner product of the function and the basis. However, although the $G_n(x)$ functions are ortho-normal, their squares are not. Thus performing an inner product on I(x) cannot extract the modal weights c_n. Gori et al. have demonstrated that performing a Fourier transform on I(x) will result in a function that is a linear combination of Laguerre-Gauss functions, which are ortho-normal functions. The resulting basis functions in the frequency domain can be seen in equation 4.2 [1]. The 'F' operator in equation 4.2 is the Fourier transform operator.

$$F\{G_n^2(x)\}(p) = \Psi_n(\pi^2 w_0^2 p^2) = L_n(\pi^2 w_0^2 p^2)\exp(-\pi^2 w_0^2 p^2 / 2) \qquad \text{(Eqn 4.2)}$$

The modal constants, c_n, can then be extracted by performing an inner product between the Fourier transform of I(x), denoted as $\widetilde{I}$ (p), and the new basis functions Ψ_n (Eqn 4.3) [1].

$$c_n = 2\pi^2 w_0^2 \int_0^\infty \widetilde{I}(p)\Psi_n(\pi^2 w_0^2 p^2)\, p\, dp \qquad \text{(Eqn 4.3)}$$

Once the c_n's are known is it possible to model the beam anywhere along the optical axis.

4.3 Performing the analysis in one-dimensional and two-dimensional discrete space

Extraction of the modes for a Hermite-Gauss beam requires that the intensity profile be analyzed with mathematical software. In this project *Matlab* was selected because of its accuracy and ease of use. In *Matlab* all data must be stored in arrays. Thus the intensity profile must be discretized. The beam must be sampled and the data stored in a two dimensional array. The conversion from continuous two-dimensional space to two-dimensional discrete space requires that the formulae for the extraction of the modal coefficients must also be discretized. The accuracy of the calculations is dependent on two principle factors. The finite discrete nature of the data in *Matlab* requires that there will be a limited numerical precision which will result in a small error between the calculated modal coefficients and the actual coefficients. The second source of error is the result of laboratory measurement. This will be discussed in the following chapter.

The challenge is to apply Gori et al.'s method to an actual beam. In an experimental setting, the intensity profile of a laser beam can be obtained by impulse point sampling the intensity over an x-y plane corresponding to a fixed value of z. Thus, it is possible to model this profile with a 2-D matrix. This can be simulated using an idealized model by constructing a two dimensional intensity profile in *Matlab.* Consider a beam with the following modal content:

$$\begin{aligned} I(x,y,z) &= 25*|u_{00}(x,y,z)|^2 + 35*|u_{01}(x,y,z)|^2 + 35*|u_{10}(x,y,z)|^2 \\ &+ 1*|u_{11}(x,y,z)|^2 + 2*|u_{02}(x,y,z)|^2 + 2*|u_{20}(x,y,z)|^2 \end{aligned} \qquad \text{(Eqn 4.4)}$$

The beam described by Equation 4.4 consists of 25% HG_{00}, 35% HG_{01}, 35% HG_{10}, 1% HG_{11}, 2% HG_{02}, 2% HG_{20}. This beam will be referred to as $BEAM_1$ in the remainder of the chapter and a surface plot of the beam's intensity profile can be found in figure 4.1. The first 3 modes produce a 'donut' shaped output, a shape that is typically observed in multimode VCSELs at certain currents. The remaining 3 modes were added to verify whether the modeling process can detect modes which are not lasing strongly. $BEAM_1$ was constructed such that its properties along the x and y axes are identical. The beam parameter $\omega_0 = 4\mu m$ is the same in both axes. Figure 4.2 is a plot of the beam radius as it propagates in free space.

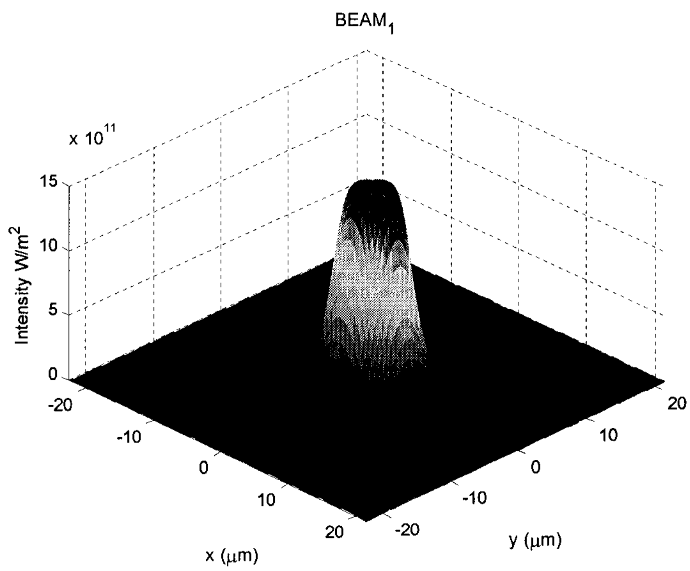

Figure 4.1: Surface plot of the intensity of BEAM$_1$.

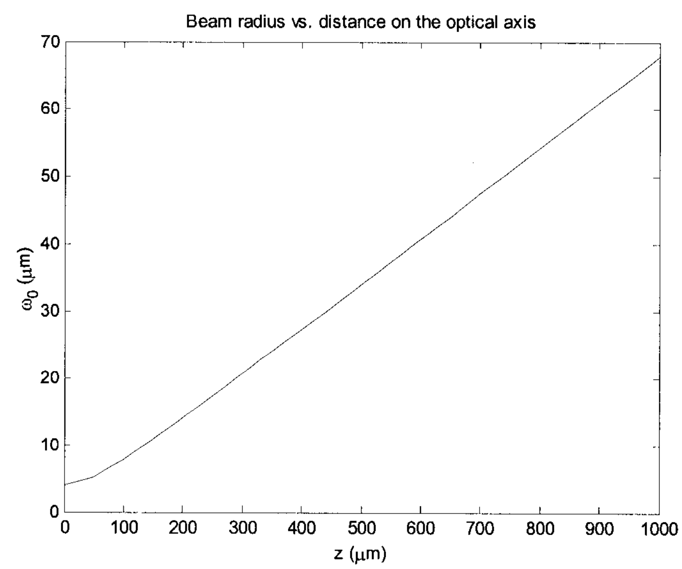

Figure 4.2: Plot of the beam radius vs. distance on the optical axis.

Given the above beam, three possible methods of modeling are presented in the following sections. As stated in the introduction two of the methods operate on one transverse dimension while the third method produces a two transverse dimensional model of the beam. Generalizing the Gori et al. method to two transverse dimensions is simple and this model is the most complete. However, there is value in applying the one-dimensional methods to a sampled beam. In practice, finding a VCSEL whose output is purely Hermite-Gauss can be challenging. The sampled beam will contain noise. It is also possible that non-uniformity in the cavity will result in non Hermite-Gauss elements in the beam. In addition, the sampling process will add noise and distortion to the acquired data. The two-dimensional modeling process will be most sensitive to these non-uniformities and may have difficulty in evaluating an accurate model. This is one of the challenges that will be discussed in greater detail in the chapter dealing with experimental results (Chapter 6). Under such circumstances it will not be possible to extract the exact modal content but if possible it is desirable to obtain a limited model of the beams shape and behaviour. A one-dimensional implementation of the method will not be affected to as great an extent as the two-dimensional method and will return limited but useful information. In addition, because calculations in two-dimensions require calculation on a $2^N x 2^N$ dimensional array versus a 2^N dimensional array for one-dimension, there is a significant increase in the required processing time and computer memory. Under certain circumstances, the information provided by a one-dimensional model may be sufficient and thus the added costs of the two-dimensional method are not necessary. It can be stated with certainty that if the modeling process fails in one-dimension it will fail in two-dimensions. Thus evaluating a model in one-dimension can serve as a test as to whether the two-dimensional method can be used. This will be of particular importance when applying the modeling process to an experimentally sampled beam. The transverse axes of the measured beam may be rotated with respect to the x and y axes of the basis functions. Under such circumstances the data must be rotated numerically, or the laser rotated and the experiment redone. Performing a 1D analysis in x and y on the corrected data can help determine if the correction rotation was done correctly.

In order to perform any of the three methods the beam must be sampled at a fixed position along the optical axis, which will be arbitrarily referred to as z_1. If possible, this position should be chosen such that it is in the near-field of the beam and it may correspond to the location of the beam waist. Because the modal content of the beam is invariant as the beam travels through an ideal optical system, the modeling process must return the same modal weights regardless of at which value of z it is performed. This will be examined in the following sections for a beam which is propagating in free-space. It should be noted that all three methods will be applied to the same theoretical beam, $BEAM_1$, described by equation 4.4.

4.4 One transverse dimensional modal extraction by taking a cross-section

In certain cases, it is convenient to model a cross-section of a beam, for example in applications where an estimate of the power distribution is needed. This method could be used to help size lenses for an optical system. The mathematical representation of taking a cross-section of the beam is represented by equation 4.5. Taking a cross-section along the x-axis is the equivalent to setting y = 0 in equation 3.14. The Gori et al. method can then be directly applied to determine the contribution of the Hermite-Gauss functions $G_n(x)$. Although it will not provide as complete a model as a full 2D model it has the advantage of being much more rapid to evaluate since only an array of N elements must be sampled and processed versus NxN elements for the two-dimensional case. Another advantage which will be explored in further detail in Chapter 5, is that noise or slight non-uniformity will not affect 1D calculations to as great an extent as 2D calculations.

$$I(x,z_1)=\sum_{n=0}^{\infty}\left[\left|G_n(x,z_1)\right|^2 * \sum_{m=0}^{\infty}\left(c_{nm} * \left|G_m(0,z_1)\right|^2\right)\right] \qquad \text{(Eqn 4.5)}$$

This method can be used to verify that any rotation in the transverse axes of the measured beam with respect to the x and y axes of the basis functions has been corrected prior to the application of the two-dimensional method. It will indicate whether a beam is composed of Hermite-Gauss modes if the model is a good fit to the data along the x or y-axis. However, it is not possible to determine the exact modal weights. This drawback occurs because taking a cross-section in x has the effect of summing all modes that have a $G_m(y)$ component in common. Therefore, the same intensity cross-section can be produced by a range of different modal weights.

The modeling process was performed for the first four $G_n(x)$ functions. The cross-section and calculated model are stored as a 512 element array. The choice of the array length will be discussed in further detail in section 4.8. Figure 4.3 plots the cross-section of $BEAM_1$. The intensity profile has been normalized to a maximum intensity of 1 so that the error between the beam and its model is plotted as a fraction of 1. The error is small relative to the magnitude of the intensity.

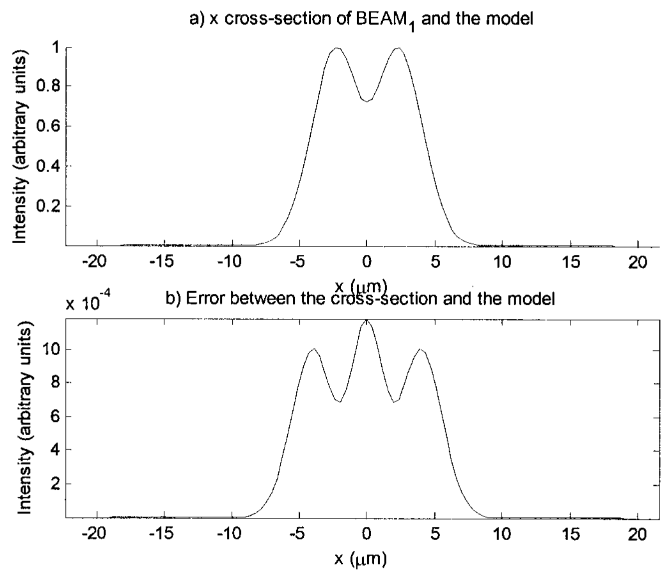

Figure 4.3: a) The x cross-section of $BEAM_1$. b)The difference of $BEAM_1$ and the evaluated model. The error is very small, thus plots of $BEAM_1$ and the model are visually indistinguishable.

In addition, modes which are zero in value along both the x and y axes will not be detected by either cross-section. For $BEAM_1$ the contributions of HG_{11} will not be detected because the value of $u_{11}(x,0) = G_n(x)G_m(0) = 0$ and $u_{11}(0,y) = G_n(0)G_m(y) = 0$ and thus is not present in either cross-section. Thus a method of detecting these missing modes must be found.

4.5 One transverse dimensional modal extraction with integration

The Gori et al. method as presented in their paper considers the beam along one transverse axis [1]. The reduction from 2D to 1D can be achieved by integrating the two transverse dimension intensity function over y thus reducing it to a function in x (Eqn 4.6).

$$I(x,z_1) = \int_{-\infty}^{\infty} \sum_{m=0}^{\infty}\sum_{n=0}^{\infty} c_{nm} \left|u_{nm}(x,y,z_1)\right|^2 dy = \sum_{n=0}^{\infty}\left(\left|G_n(x,z_1)\right|^2 * \sum_{m=0}^{\infty} c_{nm}\right) \qquad \text{(Eqn 4.6)}$$

The modal coefficients are then extracted by performing the Gori et al. method using the one transverse dimension method described in section 4.2. The intent is to obtain a one-dimensional model of the beam. This method will detect all the modal weights including those missed by the cross-sectional method, but will sum the coefficients of all the elements that have a modal component in common. In our example beam $BEAM_1$ the c_{nm} coefficients for HG_{00}, HG_{01} and HG_{02} will be added together because they have a $G_0(x,z_1)$ term. Similarly the coefficients for HG_{10} and HG_{11} will be summed. For $BEAM_1$, the calculations will return $c_0 = c_{00} + c_{01} + c_{02} = 62$, $c_1 = c_{10} + c_{11} = 36$ and $c_2 = 2$. However, having found the 1D coefficients it is not possible to determine the 2D coefficients. For example, given c_0 there is no way to distinguish between the contribution of c_{00}, c_{01} or c_{02}. (table 4.2). The values in table 4.2 are not exact due to the discrete calculation error. Figure 4.4 displays the integrated version of $BEAM_1$. Because of the form that the integrated beam takes it is not a physical representation of the beam as was the cross-sectional model. However, this method can be used to validate the cross-section method by verifying whether any modes were missed. The error between the integrated beam and the model has the same form as the error for the cross-sectional method, which is to be expected.

Modal Index (n)	Actual Modal Content	Evaluated Modal Content
0	62	62.98
1	36	35.96
2	2	1.94
3	0	0

Table 4.1: The content returned by the integration method. Although this detects all modes it is not possible to distinguish the modes individually.

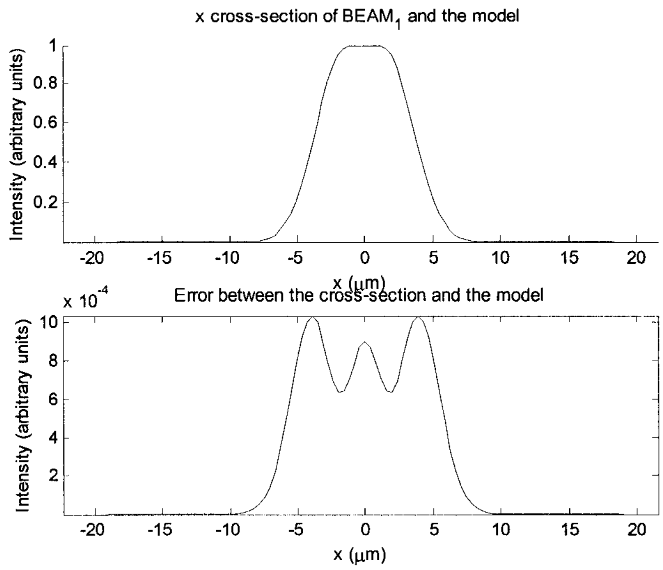

Figure 4.4: a) BEAM$_1$ after integration in y. b)The difference of BEAM$_1$ and the evaluated model. The error is very small.

From the values in table 4.2 it is possible to evaluate the value of the M^2 factor using the $G_n(x)$ content (Eqn 4.7).

$$M^2 = \sum_{n,m} b_{nm} * (2n+1) = \frac{62.98 + 3*35.96 + 5*1.94}{(62.98 + 35.96 + 1.94)} = 1.79 \qquad \text{(Eqn 4.7)}$$

4.6 Variation of the modal content due to calculation error

Observing the values in tables 4.1 it is apparent that the values returned by the modeling processes will not be exact. As stated previously, the modal coefficients remain constant as the beam propagates in free-space and the modeling process should indicate this despite the error associated with discrete mathematical calculations. There are limitations on the experimental procedure which can cause additional error to occur. As the beam propagates in free-space it becomes larger. Therefore if the area over which the beam is measured is held constant a variation in the coefficients vs. z will be observed due to the fact that the beam will be increasingly clipped. The solution to this is to increase the scan area. This may not be possible given the sampling equipment that is used, as was the case for the SNOM setup, which is described in Chapter 5. In these examples the scan area was set to 100μm x 100μm, and the vector length was held at 512x512. The variation in the dominant coefficients as a result of clipping is plotted in figure 4.5.

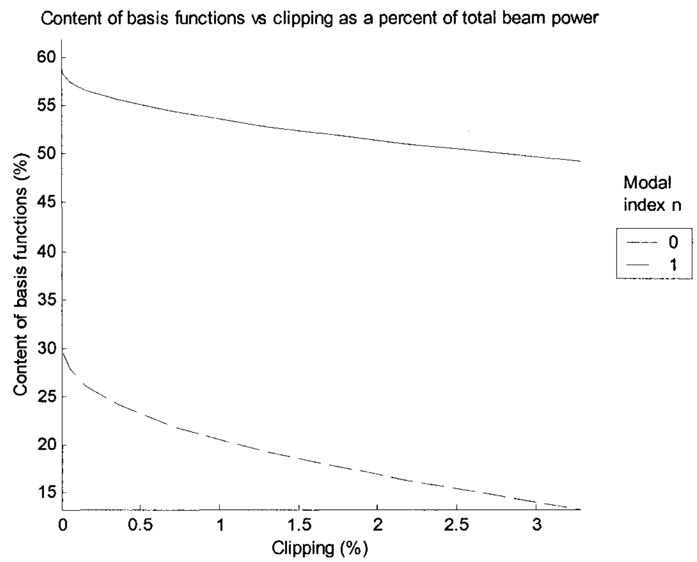

Figure 4.5: Variation of the modal content due to calculation error as the beam becomes larger and is clipped.

From figure 4.5, the error in the coefficients is severe for small power losses due to clipping. Figure 4.6 plots the x cross-section of a beam which has had 3.3% of its power content clipped.

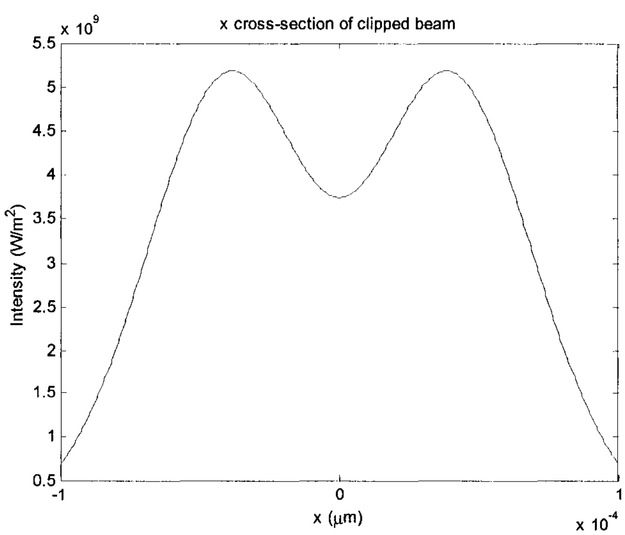

Figure 4.6: x-cross section of a beam with 3.3% of the power content clipped.

The above results indicate that the modeling process as implemented in *Matlab* can be reliably applied to one-dimensional representations of a laser beam. This allows for the method to be generalized to two-dimensions and the modal content extracted.

4.7 Two transverse dimensional modal evaluation

The most accurate model of the beam under study can be achieved by generalizing Gori et al.'s method to two transverse dimensions as suggested in their paper [1]. If the beam is a perfect combination of HG functions, as in the example given by BEAM_1 (Eqn 4.4) the modal coefficients can be obtained and the beam can then be modeled at any position z_1. Recalling the form of the intensity function (Eqn 4.9) the Gori et al. method can be generalized to two transverse dimensions by using equations 4.10 and 4.11.

$$I(x,y,z_1) = \sum_{m=0}^{\infty}\sum_{n=0}^{\infty} c_{nm}\left|u_{nm}(x,y,z_1)\right|^2 \qquad \text{(Eqn 4.9)}$$

$$\begin{aligned} F\left\{\left|u_n(x,y)\right|^2\right\}(p,q) &= F\left\{G_n^2(x)G_m^2(y)\right\}(p,q) = \Psi_n(\pi^2 w_0^2 p^2)\Psi_m(\pi^2 w_0^2 q^2) \\ &= L_n(\pi^2 w_0^2 p^2)L_m(\pi^2 w_0^2 q^2)\exp(-\pi^2 w_0^2 p^2/2)\exp(-\pi^2 w_0^2 q^2/2) \end{aligned} \qquad \text{(Eqn 4.10)}$$

$$c_{nm} = (2\pi^2 w_0^2)^2 \int_0^{\infty}\int_0^{\infty} \tilde{I}(p,q)\Psi_n(\pi^2 w_0^2 p^2)\Psi_n(\pi^2 w_0^2 p^2)\,pq\,dp\,dq \qquad \text{(Eqn 4.11)}$$

BEAM_1 and the evaluated model are stored in *Matlab* in a 512x512 array. The choice of the array length will be discussed in further detail in section 4.8. Table 4.2 compares the actual coefficients to those that are evaluated by the modeling process at the waist of the beam (position $z_1 = 0$).

Modal Index (n,m)	Actual Modal Content	Calculated Modal Content
(0,0)	25	24.95
(0,1)	35	34.98
(1,0)	35	34.98
(1,1)	1	0.95
(0,2)	2	1.96
(2,0)	2	1.96
(1,2)	0	0
(2,1)	0	0
(2,2)	0	0

Table 4.2: Comparison of the actual modal coefficients to the calculated modal coefficients at the waist.

Figure 4.7 plots the x cross-section of $BEAM_1$. It has been normalized to a maximum value of 1 so that the difference between it and the evaluated model can be plotted as a fraction of 1. The error that is apparent is the result of the discrete mathematics that was used in the calculations. It is very small so the model is visually indistinguishable from $BEAM_1$. The error can be viewed in a surface plot (Figure 4.8).

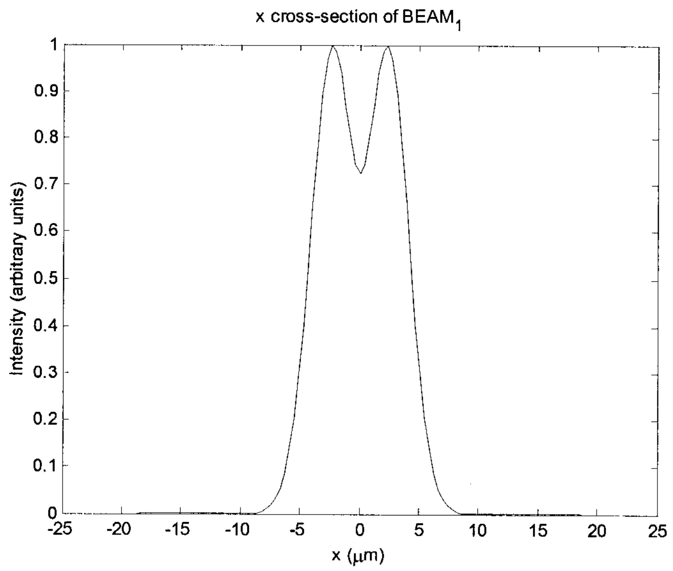

Figure 4.7: x cross-section of $BEAM_1$ at the location of the waist.

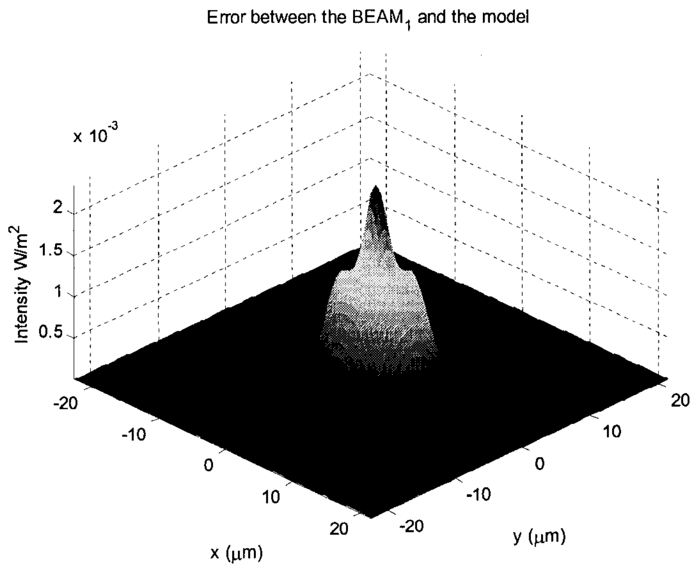

Figure 4.8: The surface plot of the difference between BEAM$_1$ and the calculated 2D model.

In section 4.5 the M^2 factor was evaluated. Now that the full modal content is know this result can be verified using equation 4.12. Thus the two-dimensional form of Gori et al.'s method can be used to solve for the M^2 value.

$$\begin{aligned} M_x^2 &= \sum_{n,m} b_{nm} * (2n+1) \\ &= \frac{(24.95+34.98+1.96)+3*(34.98+0.95)+5*1.96}{24.95+34.98+1.96+34.98+0.95+1.96} \\ &= 1.799 \end{aligned} \qquad \text{(Eqn 4.12)}$$

Figure 4.9 displays the variation due to beam clipping of the modal coefficients as the spot size increases. As was the case for the 1D case, it is observed that the 2D case will return incorrect values for the modal coefficients for small power losses due to clipping.

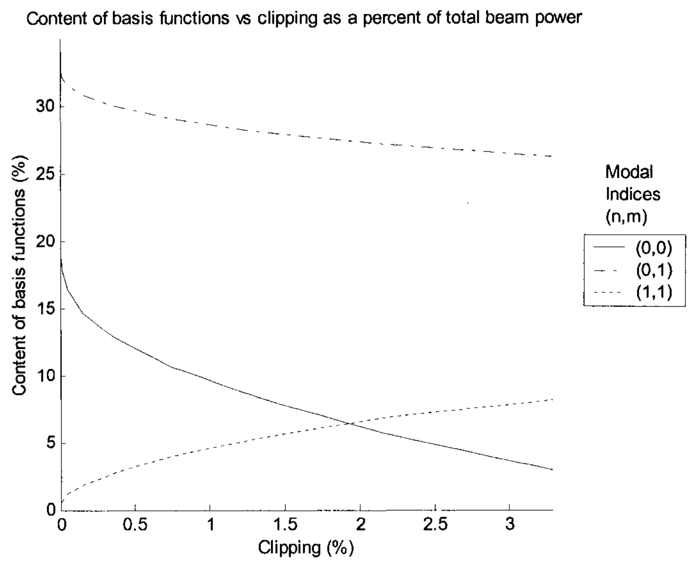

Figure 4.9: The calculated modal coefficients change due to beam clipping as the sampled beam becomes larger.

4.8 Properties of the measured data and their effect on calculation accuracy

In order to proceed with the modeling process on experimental results in Chapter 6 and 7, it is necessary to determine the sampling criteria that is needed to allow an accurate representation of the beam and correct calculations. For example, sufficient zeros must be present in the data to allow for accurate calculations and the beam must not be clipped severely.

Due to the nature of the fast Fourier transforms that are available in *Matlab* it is best to use arrays that are 2^N for the one-dimensional methods or $2^N x 2^N$ for the two-dimensional method. This does not require that the sampled data be an array whose size is a power of 2. The data can be padded with zeros to be extended to an array whose size is a power of 2. The result of the FFT will also be an array of $2^N x 2^N$, and its frequency axes span the range $-\pi$ to π. However from equation 3.14 it is seen that the integration is performed on both axes for 0 to π. Thus only a quarter of the FFT array is used, i.e. a $2^{N-1} x 2^{N-1}$ array. In order to determine what the best array size is for the calculations a test using the two-dimensional modeling method of section 4.7 was conducted for $BEAM_1$ using $2^N x 2^N$ arrays for N = 6, 7, 8, 9 and 10 to represent $BEAM_1$. In all cases the array spans an area of 100μm x 100μm and the z-position was chosen to correspond to the beam waist. The resulting modal content is tabulated in table 4.3.

Modal Index (n,m)	Actual content	Array size $2^N x 2^N$ = 64x64	Array size $2^N x 2^N$ = 128x128	Array size $2^N x 2^N$ = 256x256	Array size $2^N x 2^N$ = 512x512	Array size NxN = 1024x1024
(0,0)	25	11.01	24.95	24.95	24.95	24.95
(0,1)	35	36.12	34.99	34.98	34.98	34.98
(1,0)	35	36.12	34.99	34.98	34.98	34.98
(1,1)	2	0.00	0.95	0.95	0.95	0.95
(0,2)	1	11.26	1.92	1.96	1.96	1.96
(2,0)	1	11.26	1.92	1.96	1.96	1.96
(1,2)	0	10.47	0.0000	0.00	0.00	0.00
(2,1)	0	10.47	0.0000	0.00	0.00	0.00
(2,2)	0	6.27	0.0000	0.00	0.00	0.00

Table 4.3: Modal content as affected by array size.

From table 4.3 it can be seen that the minimum value for N is 128. When N is too small the beam is under-sampled. The FFT of the beam for N=6 is plotted in figure 4.10. The FFT is incorrect due to the limited resolution of $BEAM_l$ and thus the modeling process fails. Increasing the size of the array describing $BEAM_l$ to N=9 (figure 4.11) results in an accurate representation of the FFT and allows for modal extraction.

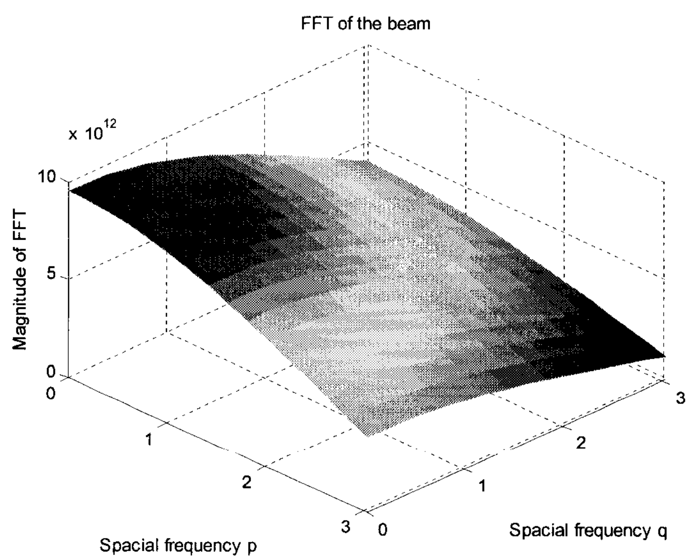

Figure 4.10: The portion of the FFT of $BEAM_l$ (64x64) from 0 to π which is used to evaluate the modal content. The low resolution of $BEAM_l$ causes this FFT to lack sufficient detail to allow modal extraction.

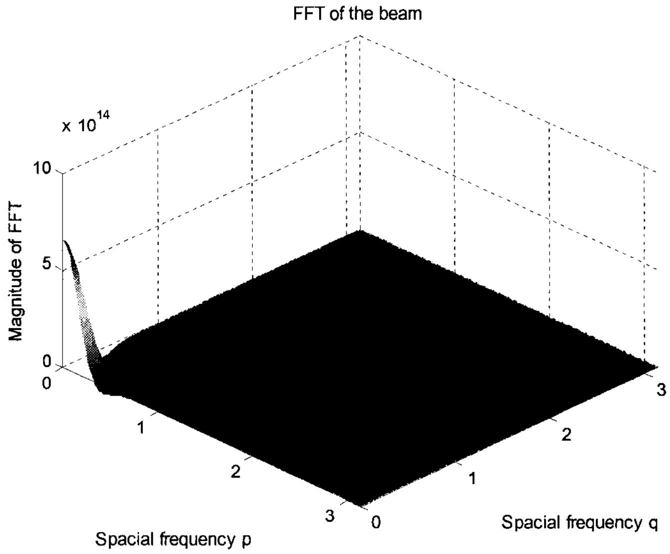

Figure 4.11: The portion of the FFT of $BEAM_1$ (512x512) from 0 to π which is used to evaluate the modal content. The FFT is accurate and modal extraction is possible.

The choice of N must be made from an integer between 7 and 10. Choosing N greater than 10 will result in long computation time and large memory usage for no appreciable gain. From table 4.3 the choice of N = 7 or 8 would have also been acceptable in this case, however using a larger value of N will result in greater accuracy as the beam diverges in free space. N = 9 was chosen because it struck a balance between accuracy and calculation time and memory usage

4.9 Determination waist parameterω_0

In the above computations it was assumed that ω_0 is known. This parameter may be estimated if sufficient knowledge of the laser cavity exists [1]. In most instances this is not possible and ω_0 must be determined experimentally. Direct measurement of ω_0 can only be achieved if the laser is biased such that only the lowest order mode is emitted under which circumstances ω_0 will correspond to the location of the $1/e^2$ points. If no prior knowledge of the modal behaviour of the laser exists, one cannot guarantee that the output is pure HG_{00} and thus ω_0 can not be determined directly from the measured data. A parameter that can be evaluated regardless of the modal content of the beam is the variance (σ^2) (Figure 4.12).

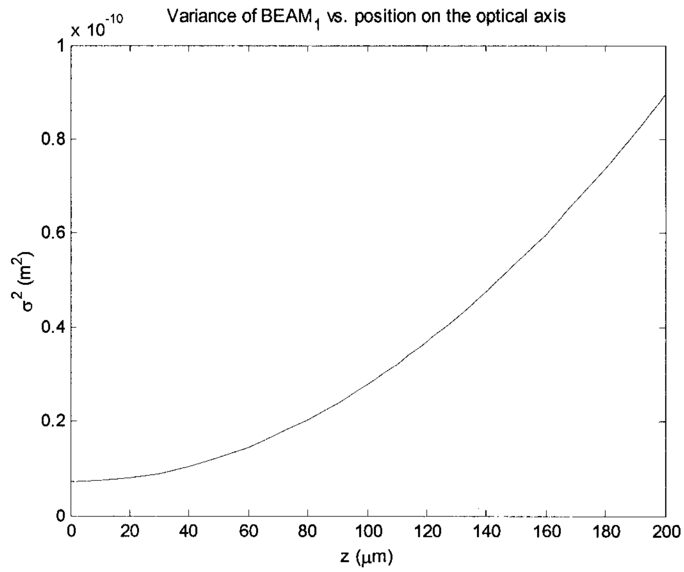

Figure 4.12: Plot of the variance of Beam$_1$ vs. position on the optical axis. The result is a parabola.

Performing a polynomial fit on the measured variance one obtains an equation of the form of equation 4.11 [3]. Therefore $\sigma^2(z)$ is a parabolic function in z as is the case for ω_0^2. The effective Rayleigh range (z_{R_eff}) can be evaluated and used to solve for ω_0 (Eqn 4.12) [3]. Knowledge of ω_0 is sufficient to solve for $\omega(z)$ at any point in free space. This provides the information required to use the modeling process described previously.

$$\sigma_x^2(z) = \sigma_x^2(z_0)\left[1+\left(\frac{z}{z_{R\_eff}}\right)^2\right] \qquad \text{(Eqn 4.11)}$$

$$\omega_0 = \sqrt{\frac{\lambda z_{R\_eff}}{\pi}} \qquad \text{(Eqn 4.12)}$$

An added result of the measurement of the variance of the beam is that it is possible to obtain the multimode waist radius from the variance (Eqn 4.13). The factor of 4 in equation 4.13 is due to the fact that the variance is taken of the intensity, which is the square of the magnitude of the electric field. From the variance we can compute the multimode beam waist radius to be 5.367 μm.

$$\omega_{0M} = \sqrt{4\sigma^2} \qquad \text{(Eqn 4.13)}$$

The proper determination of the value of ω_0 will determine whether the modeling process determines the correct modal content. To test the dependence on ω_0, the two-dimensional method of section 4.7 was applied to $BEAM_1$. $BEAM_1$ was held to be constant, that is the value of ω_0 and the modal composition was not changed. However the value of ω_0 used to construct the basis functions $u_{nm}(x,y,z_1)$ was varied from 3.5μm to 4.5μm. Recall that the correct value of ω_0 is 4μm. As is observed in figure 4.13, the result is a large variation in the computed modal weights. This variation can be explained as follows. When the value of ω_0 used for the basis functions is less that 4μm the Gaussian modes are too small in size. Since higher order modes are larger in size than lower order modes, they have a better fit to $BEAM_1$ and thus their contribution is overestimated while the percentage of the lower order modes is underestimated. The reverse occurs when the value of ω_0 used for the basis functions is greater that 4μm. Under these circumstances the lowest ordered modes are large and fit well to the size of $BEAM_1$ and are thus overestimated while the higher order modes are too large to fit $BEAM_1$ and are underestimated. Thus proper determination of ω_0 is necessary before performing beam modeling. From figures 4.14 and 4.15 the error that occurs due to the incorrect modal composition can be evaluated. The error is plotted as a fraction of the maximum intensity of $BEAM_1$.

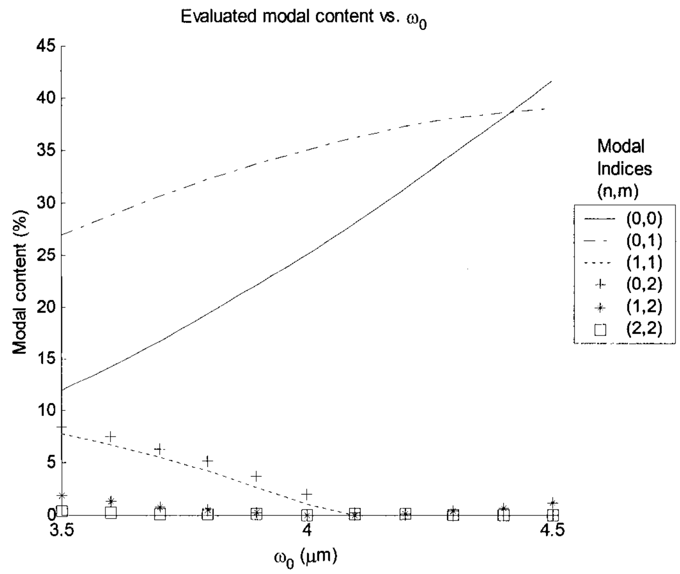

Figure 4.13: Effect on the modal coefficients if the incorrect beam waist is used. The correct values of the coefficients are found only when ω_0 for the basis functions is correct (i.e. 4μm).

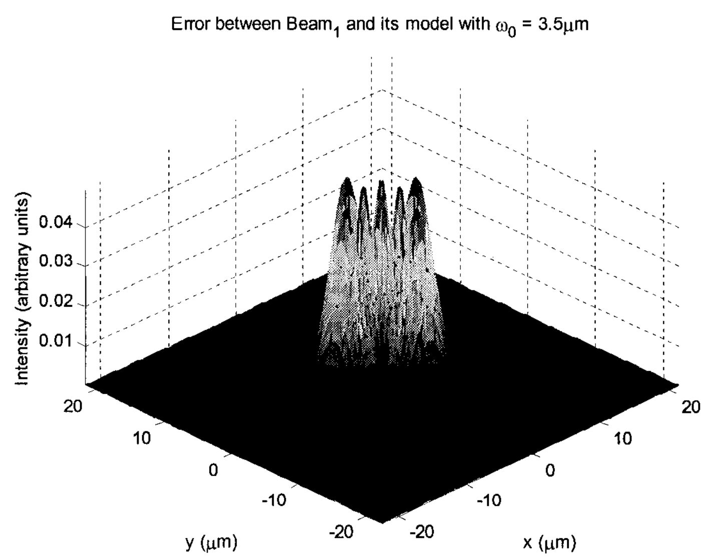

Figure 4.14: Surface plot of the error when ω_0=3.5μm.

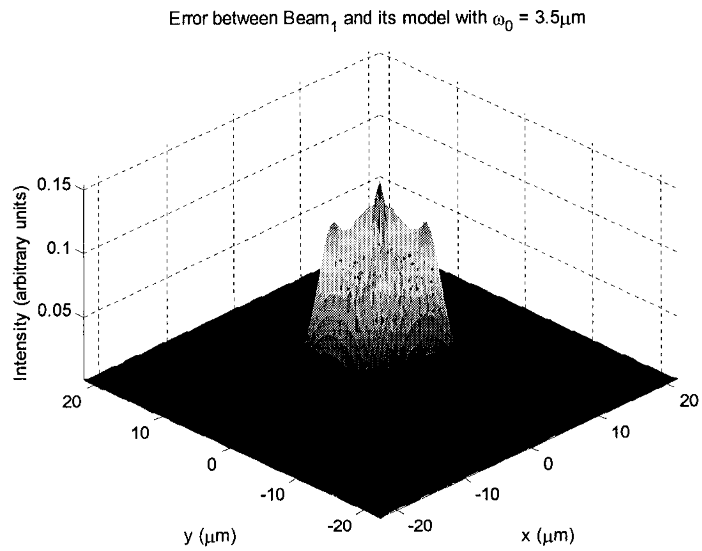

Figure 4.15: Surface plot of the error when ω_0=4.5μm.

Figures 4.14 and 4.15 it is determined that using an incorrect value for ω_0 will result in an incorrectly shaped beam model. A further test is to compare the power contained in the model with the power in BEAM$_1$. Using ω_0=3.5μm will result in the model containing 94% as much power as BEAM$_1$ and using ω_0=4.5μm will result in the model containing 122% as much power as BEAM$_1$. This compares to the model containing 99.8% of the power of BEAM$_1$ when the correct value (ω_0=4μm) is used.

4.10 Determination of the M^2 factor

The value of the M^2 factor for the beam was evaluated in previous sections to be 1.8. However from the definitions presented in chapter 3 it is known that there are methods to evaluate the value of M^2 that do not require knowledge of the modal content. The M^2 value can be computed directly from the variance of the beam (Eqn 4.14).

$$M_x^2 = \left(\frac{\omega_{0M}}{\omega_0}\right)^2 = \frac{4\pi * \sigma_x^2(z_0)}{\lambda * z_{R\_eff}} \qquad \text{(Eqn 4.14)}$$

Since M^2 can be evaluated with or without knowledge of the modal content it can be used to verify the accuracy of the three modeling processes of sections 4.4, 4.5, and 4.7. If the if an error has occurred in the modeling process the value of M^2 computed from the modal content and the value calculated from the variance will be different.

4.11 Conclusion

This chapter presented the Gori et al. method for multimode beam evaluation. Three implementations of this method were examined. The cross-sectional method was seen to produce a good model of the beam shape along both the x and y axes. It was also indicated that this method can be used to verify that a beam is indeed composed of HG modes before proceeding to the more complete two transverse dimensional method. The integration method was then presented, which allowed for the detection of modes which the cross-sectional method missed. It was also seen that this method allows for the evaluation of the M^2 factor. The two transverse dimensional method was implemented and tested for accuracy. This method allowed for the extraction of the modal content of the beam and the construction of a complete model. The knowledge gained from this in turn allowed for the determination of the properties that an experimentally sampled beam should possess in order to be properly modeled with one of the three methods. The determination of the beam waist radius ω_0 and its effect on the modal evaluation was examined. Finally, the evaluation of the M^2 factor was performed using the method to evaluate ω_0.

4.12 References

[1] F. Gori, M. Santarsiero, "Intensity-based modal analysis of partially coherent beams with Hermite-Gaussian modes", Optics Letters, Vol. 23, No. 13, July 1998, pp. 989-991.

[2] M. Santarsiero, F. Gori, R. Borghi, G. Guattari, "Evaluation of the modal structure of light beams composed of incoherent mixtures of Hermite-Gaussian modes", Applied Optics, Vol. 38, No. 25, September 1999, pp. 5272-5281.

[3] Xin Xue, Andrew G. Kirk, "Methods for estimating beam parameters of superimposed Hermite-Gaussian modes", Optics in Computing 2000, Proc. SPIE - Int. Soc. Opt. Eng, vol.4089, 2000, pp. 829-835.

5. Experimental SNOM setup

5.1 Introduction

The modeling methods presented in Chapter 4 require that the intensity profile of the VCSEL under study be measured at or near the beam waist. This can be achieved by either measuring the intensity near the surface of the VCSEL or by imaging the waist by using a lens relay system. The lens method will be examined in Chapter 7. In this chapter, the intensity is sampled near the VCSEL surface using scanning near-field optical microscopy (SNOM). SNOM was selected to acquire the intensity profiles because of its ability to resolve small details in the near-field of the VCSEL. There have been several published examples of SNOM being used to measure a VCSEL's output [1,2,3]. This chapter presents the characteristics of the components of the optical system and the acquired data before modal extraction.

5.2 Beam sampling setup

In order to perform modal extraction on the output of a VCSEL, as explained in chapter 4 and as will be done in chapter 6 and 7, an experimental setup must be assembled to measure the VCSEL's intensity profile at several currents and at different positions along the optical axis. The setup must not introduce significant noise or distortion to the measured data. In an ideal setup, an optical probe would be used to impulse point sample the beam in the near-field over an area large enough such that the intensity profile has decayed to a near-zero value. The sampling criterion is that the spatial frequency of the sampling process be at least twice that of the maximum spatial frequency in the output of the VCSEL. This allows the intensity profile to be reconstructed from the measured data. The numerical examples in Chapter 4 are the equivalent of the ideal representation of this sampling process. In practice, there are certain limitations which make a real system non-ideal. One such limitation is that it is not possible to measure the intensity with infinite spatial resolution, rather it is the power over the area of aperture the optical probe that is acquired. If the area of the aperture is too large, then a significant portion of the intensity is integrated. Features in the output which are due to high spatial frequencies will be averaged out of the sampled data. For example, consider an instance where a VCSEL is emitting in the 'donut' mode due to presence of HG_{00}, HG_{01}, and HG_{10}. When the modal content i s e valuated, t he c ontribution o f t he H G_{00} m ode w ill b e o verestimated a nd t he contributions of HG_{00} and HG_{00} underestimated which will result in a smaller dip at the center of the beam. Thus one of the first considerations is the choice of a device which can perform a good approximation of impulse point sampling. The SNOM is a good device for this task because of the small aperture of the optical probe which results in a narrow impulse response [4]. The fibers used were produced by the McGill Physics department. The fabrication process resulted in an aperture that ranged between 50nm and 200nm [5]. Since the aperture is very small, a good approximation of the intensity at any point can be acquired by dividing the power values by the area of the probe's aperture.

The experimental setup (figure 5.1) consists of the following principle components: the SNOM, a VCSEL, a current source, a power meter, and the piezo-control/data acquisition system. The following sections describe the characteristics of each device and how these affect the performance of the measurement system.

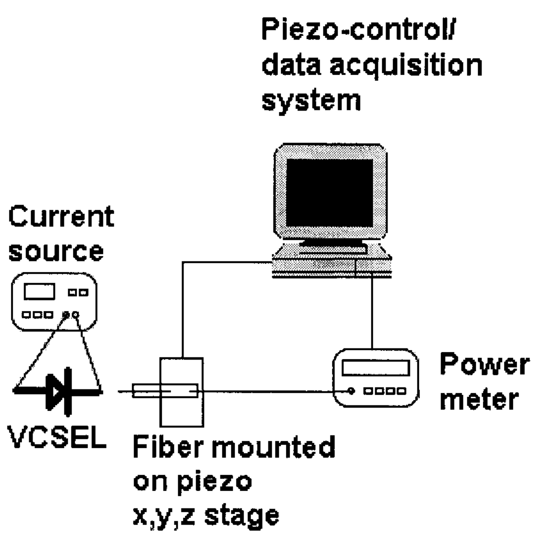

Figure 5.1: Schematic of the experimental setup used to measure the near-field intensity profiles of the VCSEL.

5.2.1 SNOM

The components of the SNOM setup are as follows: a tapered fiber (figure 5.2), a fiber holder, a piezo tube (figure 5.3) and a piezo x-y-z stage (figure 5.4). The fiber is a multimode glass fiber with 50μm core. The fiber has been adiabatically tapered using hydrofluoric acid and aluminum coated so that the aperture size of the fiber is 50nm to 200nm. The fiber is glued onto the fiber holder which is mounted on the piezo tube. The piezo has a nominal x-y travel range of 131μm x 131μm. However, it was found that distortions occurred in the scans at if the maximum area was scanned and thus the scans were limited to 61μm x 100μm. The z travel range of the piezo is 0 to 1um in 25nm steps. The SNOM is mounted on a manual x-y-z stage to provide a greater range of motion to aid in the alignment process. The feedback component of the SNOM has been disabled due to concerns that it would cause distortions in the sampled data. For this reason it was not possible to determine exactly how close the probe was to the VCSEL surface when the scans were taken.

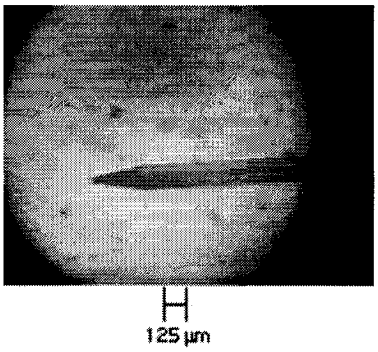

Figure 5.2: The aluminum coated fiber. The end has been etched in hydro-fluoric acid to produce a sharp tip.

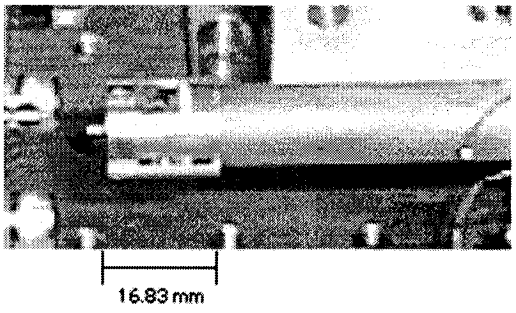

Figure 5.3: The fiber is glued on a fiber holder which is then mounted onto the piezo tube.

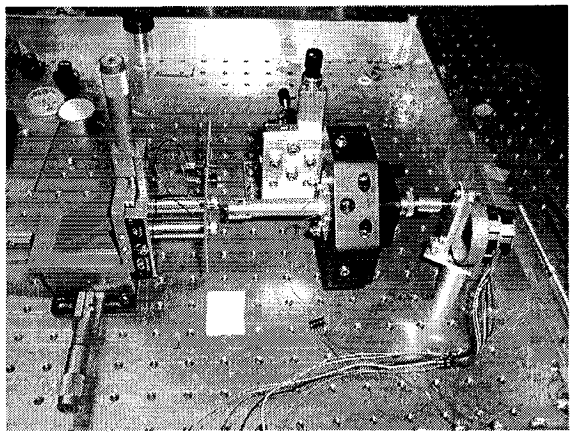

Figure 5.4: The SNOM and the VCSEL mounted, aligned and ready for a scan.

5.2.2 Piezo-control/data acquisition system

The piezo-control/data acquisition system consisted of a breakout box and a computer with the control/measurement software. The breakout box routed the control signals from the computer to the piezo stage and the data from the power meter to the computer. The control software allows the user to position the fiber using the piezo and perform a scan. The scans were performed at 1Hz per line and an array of 256x256 data points collected. The data is stored in an ASCII file for transfer to *Matlab*.

5.2.3 Current source

When operating a VCSELs in an optical system two signals may be used, a bias signal and a modulated signal containing the information to be transmitted. To measure the modal content of the beam it is necessary to observe the VCSEL under steady state conditions, thus only the bias signal is needed. A dc current source was used to drive the VCSEL directly. The current source contains feedback electronics to ensure that the current remains constant, thus the output power and modal content will not change. The current source used was an ILX Lightwave LDC3752.

5.2.4 Power meter

The fiber was attached to a bare fiber holder which was connected to a photo-detector module attached to the power meter. The device used is the Newport 2832-C power meter (figure 5.5). The photo-detector converts incident light into a current that is measured by the power meter. In order to ensure proper conversion of the current readings into optical power the wavelength must be known since the responsivity of the photo-detector varies with wavelength. Since only a small portion of the beam is sampled at any point by the optical probe the data points are in the nano-watt range. The power meter is set to read a range of power from 0 to 900nW based on the magnitude of the largest measured data point. The power meter outputs a voltage in the 0 to 5V range, which is then read by the data acquisition system. The power is mapped onto the voltage linearly. Care must be taken when choosing the upper value of the power range. A value that is too large compared to the magnitude of the samples results in insufficient resolution. A value for maximum power that is too small will cause the meter to saturate and an erroneous profile will be obtained.

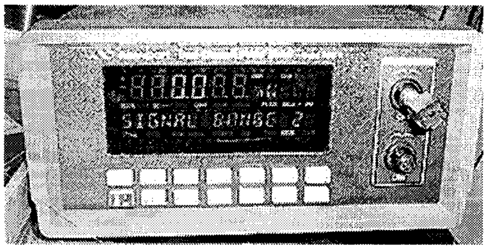

Figure 5.5: The Newport 2823-C power meter with fiber attached connector/photo-detector.

5.2.5 VCSEL

The device used is a GaAs VCSEL with a nominal output wavelength of 850nm (figure 5.6). It is fabricated by Honeywell and the model number is HFE4080-321. Table 5.1 contains the principle characteristics of the VCSEL as indicated on the device specification sheet provided by Honeywell [6].

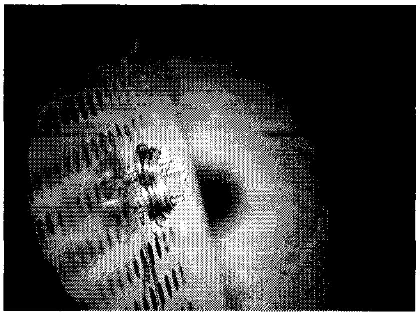

Figure 5.6: VCSEL mounted on a PCB.

VCSEL Parameter	Test condition	Min.	Typ.	Max.	Units
Peak operating current			12	20	mA
Optical power output	I = 12mA	0.9	1.8	3.6	mW
Threshold current		1.5	3.5	6	mA
Threshold current temperature variation	T = 0^oC to 70^oC	-1.5		1.5	mA
Slope efficiency	P_0 = 1.3mW	0.1	0.25	0.4	mW / mA
Slope efficiency temperature variation	T = 0^oC to 70^oC		-0.5		% / ^oC
Peak wavelength temperature variation	I = 12mA		0.06		nm / ^oC
Spectral Bandwidth, RMS	I = 12mA			0.85	nm
Rise and fall times	Prebias above threshold, 20%-80%		100	300	ps
Relative intensity noise	1 GHz BW, I = 12mA		-128	-122	dB / Hz
Beam divergence ($1/e^2$)		5	15	20	degrees

Table 5.1: Principle characteristics of the VCSEL (HFE4080-321) as indicated on the device specification sheet provided by Honeywell.

Examining the information from table 5.1, some of the characteristics that were reported in Chapter 2 can be observed. The spectral bandwidth is 0.85nm. Recall that each transverse mode will occur at a slightly different wavelength. Because the bandwidth is very small when compared to 850nm, the peak wavelength of the laser, the VCSEL can be considered to lase at a single longitudinal mode. The change in the emitted wavelength as a function of temperature is also quite small. The temperature also has the effect of raising the threshold current of the laser [7]. The beam divergence, defined in this case as the angle between the $1/e^2$ points, is given as a range from 5^0 to 20^0. As the current is increased the beam divergence will increase as higher order transverse modes begin to lase.

Figures 5.7 and 5.8 are plots of the current versus voltage and the power versus current for the VCSEL under test. As expected the current has an exponential behaviour with respect to voltages above the threshold voltage and the power increases linearly with current above the threshold current. From the L-I curve, the following values are found for threshold current and slope efficiency, respectively, I_{th} = 3.1mA and η = 0.4mW/mA. These results are within the nominal ranges reported in table 5.1 for this HFE4080-321 VCSEL model.

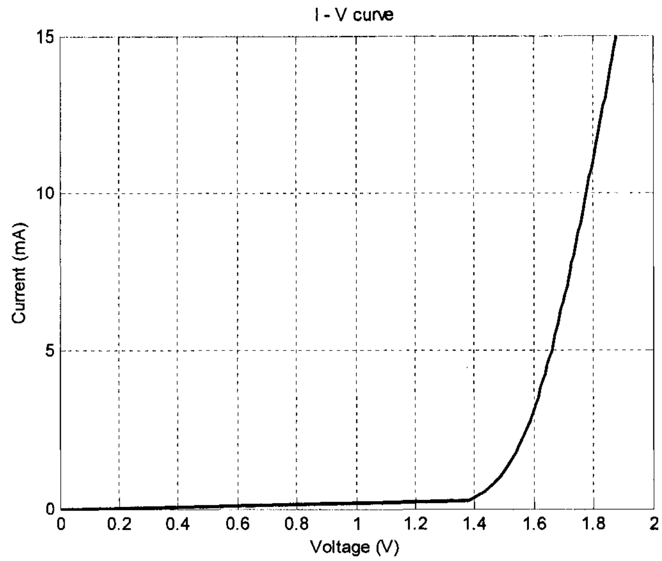

Figure 5.7: Measured current vs. voltage.

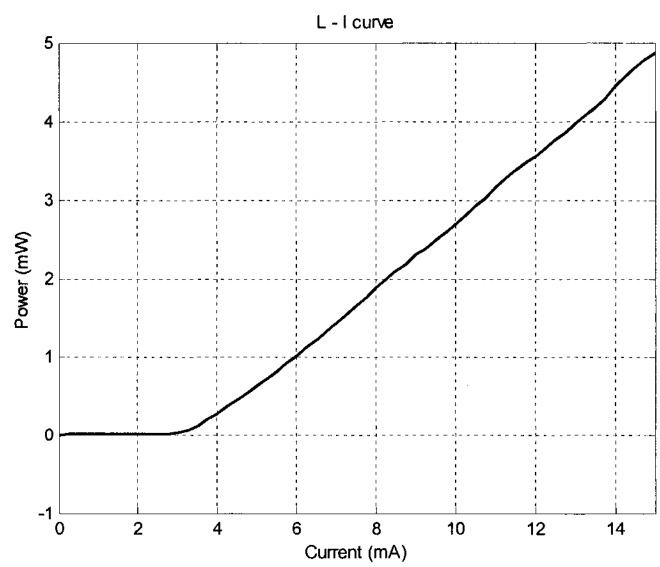

Figure 5.8: Measured power vs. current.

The VCSEL is packaged in a protective casing with a metal cap containing a plastic window to allow the light to escape. It was found that the window distorted the beam's shape. It also prevented the optical probe from approaching the surface of the VCSEL. Thus, the cap was removed. Scans were then performed within approximately 100μm of the VCSEL's surface (figure 5.9). The VCSEL was mounted on a plastic circuit board which contained the wires connected to the current source. The PCB was mounted on a manual x-y-z stage to aid in the alignment of the system.

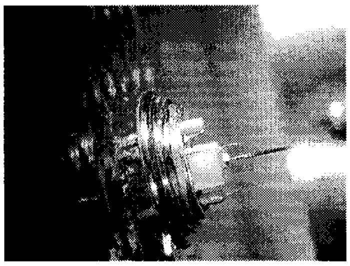

Figure 5.9: The SNOM fiber is positioned for a scan of the VCSEL.

5.3 Measured data

The setup described in the previous section was used to sample the output of the VCSEL at 4 z-positions for currents of 4, 5, 10 and 12mA. The intensity profiles presented in this section were measured in July 2002 by Camille Brès and Carole Haddad. The profiles are plotted in figures 5.10 to 5.13. As the current is increased the size of the beam increases and the presence of higher order modes can be deduced from the shape of the beam.

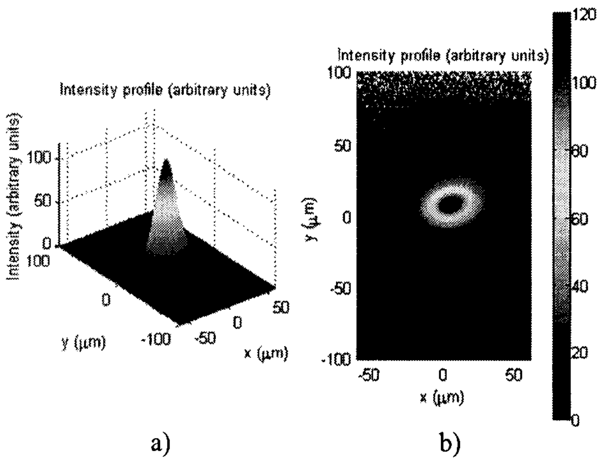

Figure 5.10: Intensity profile at I = 4mA. a) angled view and b) top view.

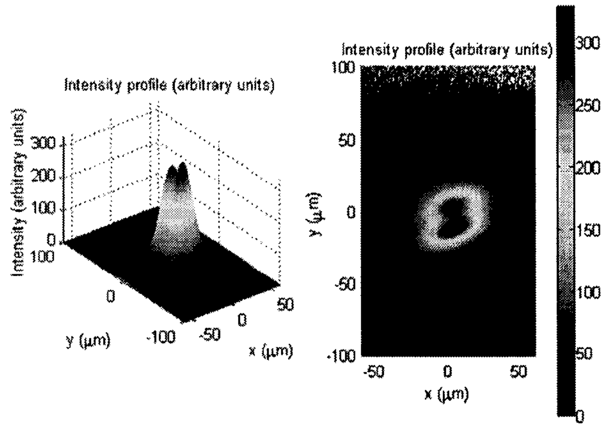

a) b)

Figure 5.11: Intensity profile at I = 5mA. a) angled view and b) top view.

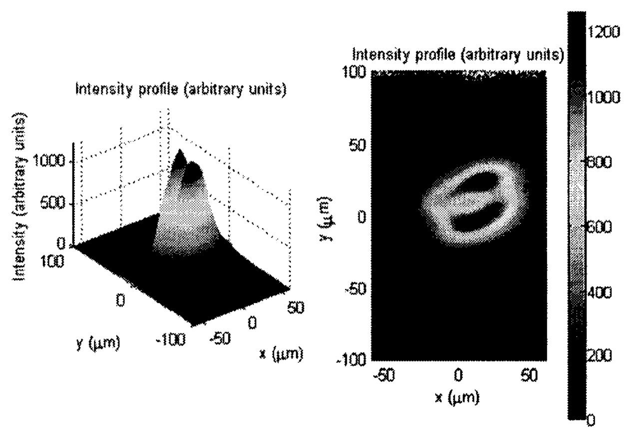

a) b)

Figure 5.12: Intensity profile at I = 10mA. a) angled view and b) top view.

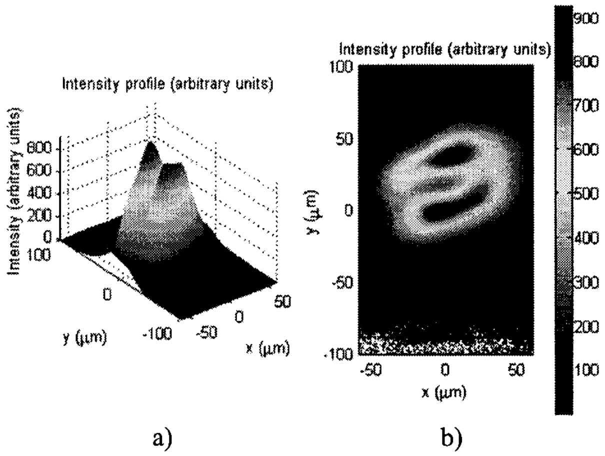

Figure 5.13: Intensity profile at I = 12mA. a) angled view and b) top view. Note that the intensity is not to the same scale as the previous 3 plots because the z-position is different for 12mA, than for the other currents.

The shape of the intensity profiles emitted by the VCSEL suggests that HG modes are the appropriate model to be used. However, the outputs have non-symmetric elements. In the absence of significant distortions caused by the sampling process it can be deduced that the variation from an ideal HG beam is caused by the anisotropy in the VCSEL structure [8]. Thus it must be recognized that the numerical models that are computed in chapter 6 are approximate at best. It must be emphasized that for VCSEL to have well defined HG modes it must be of high quality. Half a dozen VCSELs, of two different model types, were tested using the SNOM and the device with the most ideal output was selected. It can be expected that as VCSEL technology continues to advance the match of the actual modal content to ideal HG modes will improve.

Since modal extraction requires that complex calculations to be performed on the experimental data certain corrections must be made. Observing the orientation of the symmetry in the plots it is observed that the transverse axes of the data are rotated with respect to the x and y axes of the scans. Thus a correction rotation is applied to the data before modal extraction is performed in chapter 6. Most of the noise contained in the acquired data was on the outer periphery of the data, which suggests that it is due to spontaneous emissions from the outer edges of the cavity [9]. Some of the noise that exists along the outer edges of the scans can be removed. The zero value of the data must also be verified. It is possible that dark current in the photo-detector will cause a slight offset in all the data [10]. To increase the accuracy of the calculations extra zeros can be added in *Matlab* to the exterior edges of the data.

Despite the adjustments that can be made there are some issues that can not be compensated for and thus will hinder evaluation of the modes. A difficulty in performing scans was the impossibility of knowing the exact z-position due to the absence of feedback in the SNOM. The scan at I = 12mA was taken slightly further from the VCSEL than those at I = 4, 5, 10mA which accounts for the lower peak intensity observed for 12mA in figure 5.12. However, this does not influence the modal content. The intensity profiles are a time average measurement because the scans take a few minutes to complete. Thus, if there are any changes in the output of the laser during a scan the acquired data will be distorted. Thus, the temperature and biasing of the VCSEL must be stable to ensure that the experiment is repeatable.

256 x 256 points were sampled in x and y and the scan area was 61μm x 100μm. This resulted in a sample spacing of 239nm in x and 392nm in y. The limits on the scan area was imposed by the behaviour of the piezo translation stage. The scans at 10mA and 12mA were thus clipped in the x direction due to the lack of range.

5.4 Conclusion

This chapter presented the experimental setup constituting the SNOM and its associated equipment. The data presented exhibits sufficient characteristics to suggest that an attempt to evaluate a Hermite-Gauss model can be made in the following chapter. The accuracy of any model will depend on the quality of the experiments that were performed to acquire the data. Although there are issues that presented themselves in the course of experimentation, it will be demonstrated in chapter 6 that pertinent information can be evaluated from the intensity profiles obtained from the SNOM.

5.5 References

[1] J.A. DeAro, K. D. Weston, R. W. Herrick, P. M. Petroff, S. K. Buratto "Near-field scanning optical microscopy of cleaved vertical-cavity surface-emitting lasers", Semicond. Sci. Technol., Vol.13, No. 12, December 1998, pp. 1364-1367.

[2] K.J. Knopp, D.H. Christensen, G. Vander Rhodes, J.M. Pomeroy, B.B. Goldberg, M. Selim Unlu, "Spatio-Spectral Mapping of Multimode Vertical Cavity Surface Emitting Lasers", Journal of Lightwave Technology, Vol. 17, No. 8, 1999, pp. 1429-1435.

[3] I. Horsch, R. Kusche, O. Marti, B. Weigl, K.J. Ebeling, "Spectrally resolved near-field mode imaging of vertical cavity semiconductor lasers", J. Appl. Phys., Vol.79, No.8, pt.1, 1996, pp. 3831-3834.

[4] E. Betzig, J.K. Trautman, T.D. Harris, J.S. Weiner, R.L. Kostelak, "Breaking the Diffraction Barrier: Optical Microscopy and a Nanometric Scale", Science vol. 251, no 5000, 1991, pp.1468-1470.

[5] C. Brès, C. Haddad, private communication, May 2002.

[6] Fiber optic components, GaAs 850nm VCSEL, HFE4080-321, see: http://content.honeywell.com:80/vcsel/pdf/4080-321.pdf

[7] C. Wilmsen, H. Temkin, L.A. Coldren, *Vertical-Cavity Surface-Emitting Lasers*, Cambridge University Press, New York, New York, 1999, pp. 198-200.

[8] C. Degen, B. Krauskopf, G. Jennemann, I. Fischer., W. Elsaber, "Polarization selective symmetry breaking in the near-fields of vertical cavity surface emitting lasers", J. Opt. B: Quantum Semiclass. Opt. Vol. 2, No. 4, 2000, pp. 517-525.

[9] O. Buccafusca, J. L. A. Chilla, et al., "Transient Response of Vertical-Cavity Surface Emitting Lasers of Different Active-Region Diameters", IEEE Journal of Quantum Electronics, Vol. 35, No. 4, April 1999, pp. 608-615.

[10] G, Keiser, *Optical Fiber Communications*, 3rd ed., McGraw-Hill, Toronto, Ontario, 2000, pp. 252-257.

6. Extraction of HG modes from experimental data acquired by SNOM

6.1 Introduction

In Chapter 4, it was demonstrated that the modes in the simulated output of a multimode VCSEL could be extracted. The challenge is to apply the theoretical approach to an actual VCSEL. There are several factors that will determine whether it is possible to apply the Gori et al. method to a particular VCSEL. It must be determined whether Hermite-Gauss or Laguerre-Gauss functions are the appropriate basis functions. For the VCSEL under study, a Hermite-Gauss basis is chosen based in part on the knowledge that the cavity is rectangular. Since the cavity is very small, small non-uniformities in the cavity can greatly affect the laser's output [1]. In the case where large stable cavity lasers are under study, it is reasonable to assume that the modes will be close to the ideal Hermite-Gauss modes. Finding a VCSEL which is close to the ideal case can be more difficult. Individual VCSELs of the same model type may have outputs which can be quite different, although as fabrication techniques continue to evolve it can be expected that more VCSELs will exhibit HG outputs.

In this chapter, the intensity profiles measured with the SNOM (Chapter 5) will be analyzed using the Gori et al. technique [2,3]. The objectives of this chapter are twofold, to demonstrate that a consistent model of the laser output can be constructed and to study the modal behaviour versus current. The purpose of the modeling process is thus to verify if a VCSEL, which appears to exhibit an output resembling that of a superposition of Hermite-Gauss modes, can be effectively modeled by Hermite-Gauss functions. In order for the modeling process to be successful, the model must match the expected behaviour of the beam as it propagates through an optical system. This chapter is structured as follows. The cross-sectional method is used to model the x and y axes cross-sections of the beam. The integration method is used to calculate the summed modal content and the M^2 factor. The two transverse dimensional method is then used on an intensity profile and compared to the integration method.

6.2 Modeling of a VCSEL's output

6.2.1 Cross-sectional method

The output of the VCSEL under study was sampled using the SNOM at currents of 4mA, 5mA, 10mA, and 12mA. For each current the output was sampled at four positions separated by 10μm. The purpose of calculating the model at several z-positions was two-fold. Because this experiment was a test of the modeling process it was necessary to see if a constant model could be evaluated as the beam diverged in free space. The second reason, is that when constructing a model it is best to take an average of the modal percentages over several z-positions to minimize the effect that measurement error may have.

The purpose of commencing with the one-dimensional method is that it is inherently simpler to construct a one transverse dimensional model than a two transverse dimensional model. Of the three methods presented in chapter 4, the cross-sectional method is least sensitive to distortion in the beam. Thus, if the modeling process fails in one-dimension it can not succeed in two. Examining the cross-section of the beam is also important to allow for the determination of the orientation of the x and y-axis. The x and y axis of the VCSEL must correspond exactly with the x and y-axis of the scanning stage. If a rotation exists, either the VCSEL must be rotated or the acquired data must be rotated numerically in *Matlab*. Examining the x and y cross-sections and computing a one-dimensional model can aid in the alignment of the system. If the cross-sections are found not to be HG, this can indicate that the choice of x and y-axes was poorly made.

In this section the cross-sections of the intensity profiles in x and y are decomposed using the HG basis functions for one dimension (Eqn 6.1). As discussed in chapter 4, this allows for the construction of a limited model of the beam. The mathematical form of the cross-section (see Eqn 4.5 reprinted below for convenience) indicates that it is not possible to determine the exact modal content. However, the model will provide an accurate description of the beam shape along the axes and serves as an indicator of what modes exist.

$$G_n(x,z_1) = \left(\frac{2}{\pi\omega^2(z_1)}\right)^{\frac{1}{4}} * \frac{1}{\sqrt{2^n n!}} * H_n\left(\frac{x\sqrt{2}}{\omega(z_1)}\right) * \exp\left(\frac{-x^2}{\omega^2(z_1)}\right) \qquad \text{(Eqn 6.1)}$$

$$I(x,z_1) = \sum_{n=0}^{\infty}\left[\left|G_n(x,z_1)\right|^2 * \sum_{m=0}^{\infty}\left(c_{nm} * \left|G_m(0,z_1)\right|^2\right)\right] \qquad \text{(Eqn 4.5)}$$

There are 8 tables in this section (tables 6.1 to 6.8). Each table corresponds to the one-dimensional model (in x or y) for one of the four currents (4mA, 5mA, 10mA or 12mA). The tables contain the percentage contribution of each basis function to the total model. The indices, n for x and m for y, indicate the order of $G_n(x,z_1)$ or $G_m(y,z_1)$. As was stated previously, the modal content is constant over distance and thus the calculated percentages should reflect this. For each index value, the percentages in that row of the table should be the same. Looking at the tables one observes that there are small differences in the modal content as the z position is changed. There are several reasons why this occurs. Firstly, since $\omega(z)$ must be determined experimentally its value will not be exact. This in turn will result in some error in the model. The second error type is due to random noise that is present in the acquired data will result in small changes in the shape of the beam over time, which in turn will change the model slightly. The third source of error will occur if the beam begins to be clipped significantly. If a significant portion of the beam is lost insufficient information exist to allow for an accurate model to be evaluated. The fourth source of error results from distortions in the measured beam shape at different z-positions. This will be a factor because the sampling equipment will not be perfectly aligned with the VCSEL and thus the beam will not be measured at the exact position and angle that is assumed by the mathematical model. Figures 6.1 to 6.8 plot the cross-section of the VCSEL beam. The intensity profiles have been normalized to a maximum intensity of 1 so that the error between the beam and its model is plotted as a fraction of 1.

The examination of the results begins with the tables for the x and y cross-sections at 4mA (tables 6.1 and 6.2).

Modal Index n	$G_n(x)$ content at position z_1	$G_n(x)$ content at position z_1+10μm	$G_n(x)$ content at position z_1+20μm	$G_n(x)$ content at position z_1+30μm	Average	Standard deviation as a % of the mean
0	61.9%	61.7%	57.7%	58.8%	60.0%	3.5%
1	23.4%	24.1%	25.4%	25.0%	24.5%	3.7%
2	8.9%	9.1%	10.8%	10.0%	9.8%	9.0%
3	3.7%	3.4%	4.4%	4.2%	3.9%	11.7%
4	1.5%	1.3%	1.5%	1.4%	1.4%	6.7%
5	0.6%	0.3%	0.2%	0.1%	0.3%	72.0%

Table 6.1: Modal content in x for I = 4mA.

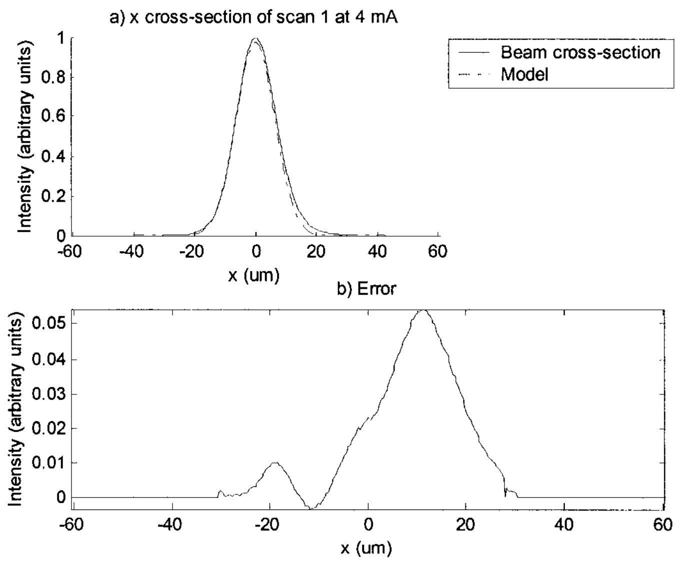

Figure 6.1: a) x cross-section of the beam and the evaluated model for z-position z_1. b) The error was computed by subtracting the cross-section and the model.

Modal Index m	$G_m(y)$ content at position z_1	$G_m(y)$ content at position z_1+10μm	$G_m(y)$ content at position z_1+20μm	$G_m(y)$ content at position z_1+30μm	Average	Standard deviation as a % of the mean
0	95.3%	90.8%	88.6%	92.8%	91.9%	3.1%
1	0.0%	1.6%	6.0%	3.2%	2.7%	94.8%
2	4.3%	5.5%	3.0%	2.1%	3.7%	40.0%
3	0.0%	1.5%	1.5%	1.9%	1.2%	68.4%
4	0.1%	0.2%	0.8%	0.0%	0.3%	130.7%
5	0.2%	0.3%	0.0%	0.0%	0.1%	120.0%

Table 6.2: Modal content in y for I = 4mA.

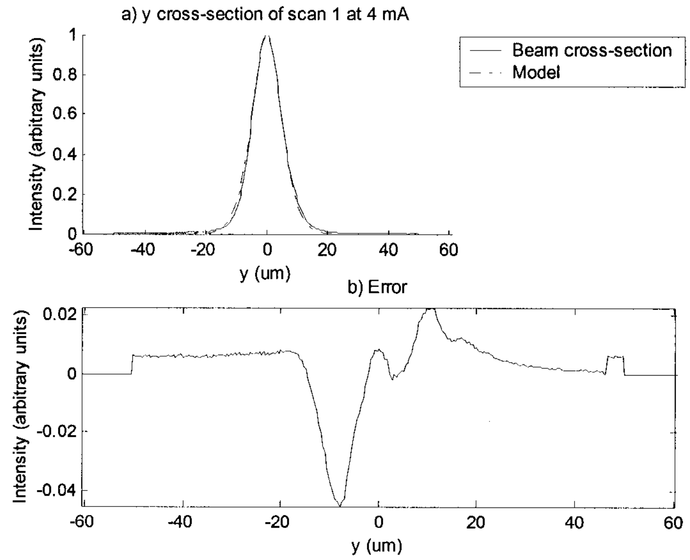

Figure 6.2: a) y cross-section of the beam and the evaluated model for z-position z_1 . b) The error was computed by subtracting the cross-section and the model.

The experimental data is not perfectly Hermite-Gauss because it is not perfectly symmetric about the origin. However, the model is perfectly symmetric since it is purely HG, this results in a non-symmetric error curve (figures 6.1 (b) and 6.2 (b)). The evaluated model has a reasonably good fit to the experimental data (figures 6.1 (a) and 6.2 (a)) and the error is small relative to the scale of the intensity profiles (figures 6.1 (b) and 6.2 (b)).

From tables 6.1 and 6.2 it is noted that the dominant contribution in both axes comes from c_0. The largest variation in the modal percentages also occurs in c_0. For the x-axis the c_0 modal content ranges from 57.5% to 61.9% and for the y-axis the c_0 modal content ranges from 88.6% to 95.3%. From the plots of the beam at the different positions it can be determined that the beam has not been clipped nor is noise a significant factor. Furthermore, there does not appear to be significant distortion in the beam shape at any of the four z-positions. Thus the choice of $\omega(z)$ will be the greatest cause of the variation of the modal percentages.

Comparing the results for the x and y cross-sections reveals two details of note. The beam waist parameter ω_0 is not the same in x and y. When VCSELs are manufactured the cavities are designed to be square. However, due to the small size of the laser it is to be expected that the cavity will not be perfectly square. Thus the ω_0's for x and y will be close but not identical. Anisotropy in the cavity due to strain or non-isotropic injection of current into the cavity will also influence the beam shape. The second observation is that the modal content is not the same in both x and y. At 4mA the y cross-section is nearly perfectly Gaussian while the x cross-section has a larger contribution from higher order components.

Tables 6.3 and 6.4 contain the x and y models respectively for the VCSEL output when biased at 5mA.

Modal Index n	$G_n(x)$ content at position z_1	$G_n(x)$ content at position z_1+10μm	$G_n(x)$ content at position z_1+20μm	$G_n(x)$ content at position z_1+30μm	Average	Standard deviation as a % of the mean
0	55.2%	54.6%	53.2%	53.8%	54.2%	1.6%
1	28.9%	29.7%	29.7%	30.1%	29.6%	1.7%
2	11.1%	11.4%	12.4%	12.8%	11.9%	6.8%
3	3.4%	3.5%	4.2%	3.4%	3.6%	10.7%
4	1.2%	0.8%	0.6%	0.0%	0.7%	76.9%
5	0.2%	0.0%	0.0%	0.0%	0.1%	200.0%

Table 6.3: Modal content in x for I = 5mA.

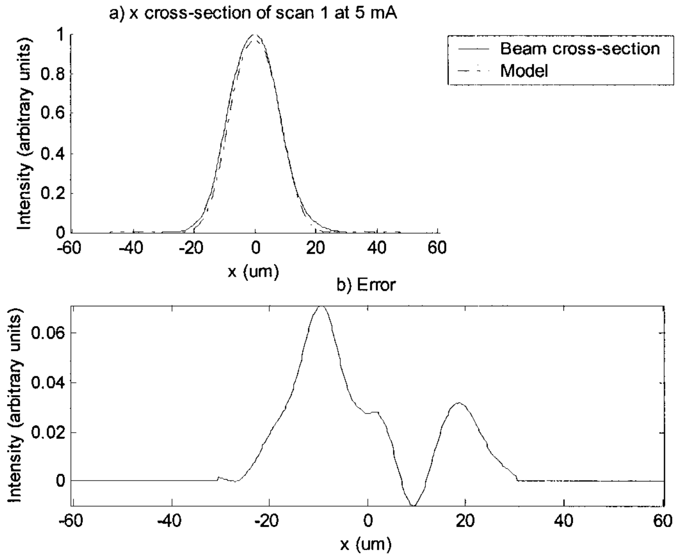

Figure 6.3: a) x cross-section of the beam and the evaluated model for z-position z_1. b) The error was computed by subtracting the cross-section and the model.

Modal Index m	$G_m(y)$ content at position z_1	$G_m(y)$ content at position $z_1+10\mu m$	$G_m(y)$ content at position $z_1+20\mu m$	$G_m(y)$ content at position $z_1+30\mu m$	Average	Standard deviation as a % of the mean
0	55.2%	53.1%	50.2%	53.8%	53.1%	4.0%
1	39.7%	42.7%	44.0%	42.8%	42.3%	4.3%
2	0.0%	0.0%	2.4%	0.0%	0.6%	200.0%
3	3.8%	1.5%	0.0%	1.1%	1.6%	99.9%
4	1.3%	2.0%	2.5%	1.1%	1.7%	37.4%
5	0.0%	0.6%	0.9%	1.2%	0.7%	75.9%

Table 6.4: Modal content in y for I = 5mA.

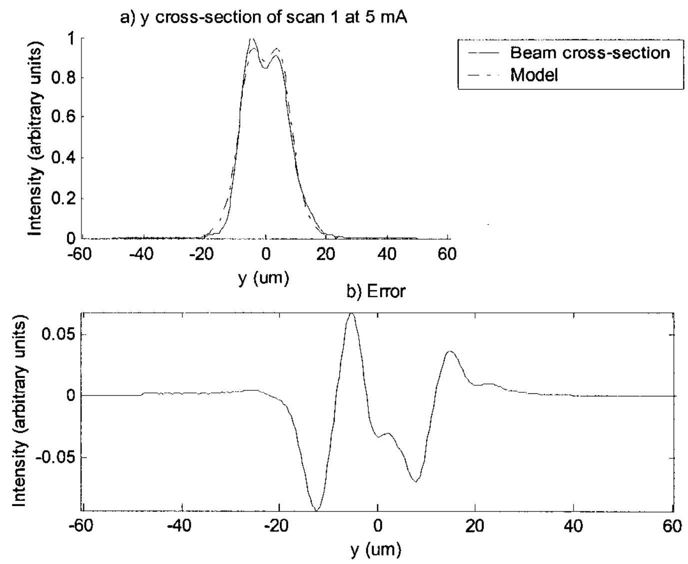

Figure 6.4: a) y cross-section of the beam and the evaluated model for z-position z_1. b) The error was computed by subtracting the cross-section and the model.

Comparing I = 5mA to I = 4mA for both x and y reveals the following. The increase in bias current results in increased output power. There is also an increase in the contribution of the higher order modes to the output. Comparing x and y, the change in modal content is most pronounced in y. The presence of higher order modes results in the a dip in the center of the y cross-section.

Tables 6.7 and 6.8 contain the x and y models respectively for the VCSEL output when biased at 10mA.

Modal Index n	$G_n(x)$ content at position z_1	$G_n(x)$ content at position z_1+10μm	$G_n(x)$ content at position z_1+20μm	$G_n(x)$ content at position z_1+30μm	Average	Standard deviation as a % of the mean
0	26.4%	24.2%	22.5%	20.9%	23.5%	10.0%
1	62.0%	60.6%	58.4%	61.9%	60.7%	2.8%
2	11.4%	15.2%	19.1%	17.2%	15.7%	21.0%
3	0.0%	0.0%	0.0%	0.0%	0.0%	0.0%
4	0.2%	0.0%	0.0%	0.0%	0.1%	200.0%
5	0.0%	0.0%	0.0%	0.0%	0.0%	0.0%

Table 6.5: Modal content in x for I = 10mA.

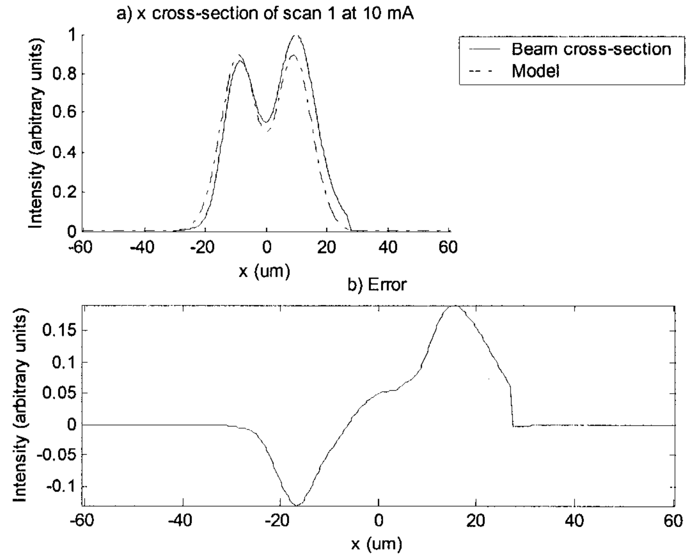

Figure 6.5: x cross-section of the beam and the evaluated model for z-position z_1. b) The error was computed by subtracting the cross-section and the model.

Modal Index m	$G_m(y)$ content at position z_1	$G_m(y)$ content at position z_1+10μm	$G_m(y)$ content at position z_1+20μm	$G_m(y)$ content at position z_1+30μm	Average	Standard deviation as a % of the mean
0	13.7%	13.0%	10.0%	11.9%	12.2%	13.3%
1	54.4%	59.2%	54.8%	59.2%	56.9%	4.7%
2	19.0%	18.0%	23.6%	20.2%	20.2%	12.1%
3	7.7%	6.0%	7.2%	5.5%	6.6%	15.5%
4	2.3%	2.2%	2.8%	2.3%	2.4%	11.3%
5	3.0%	1.7%	1.7%	0.8%	1.8%	50.3%

Table 6.6: Modal content in y for I = 10mA.

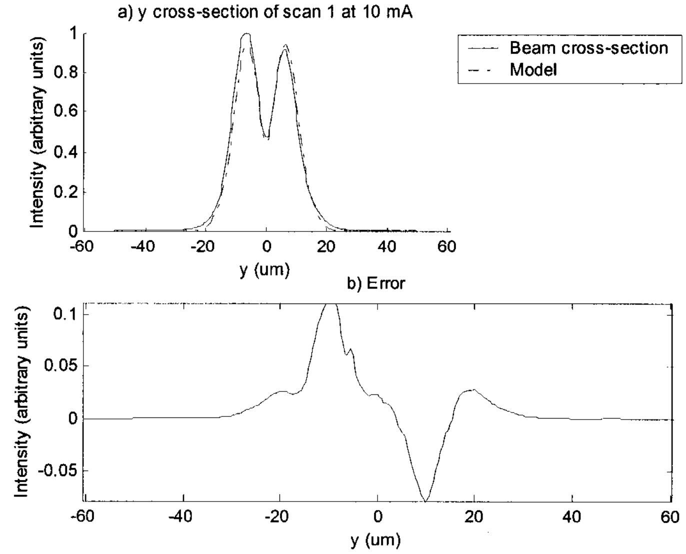

Figure 6.6: y cross-section of the beam and the evaluated model. b) The error was computed by subtracting the cross-section and the model.

At 10mA $G_1(x)$ and $G_1(y)$ dominate the laser emission. The error between the cross-section and the model is much larger (figures 6.5 (b) and 6.6 (b)). One reason for this is that the beam is becoming increasingly non-symmetric about the transverse axes. The Hermite-Gauss model can not produce non-symmetric shapes thus the error is large.

Tables 6.9 and 6.10 contain the x and y models respectively for the VCSEL output when biased at 12mA. Note that the initial z-position is denoted as z_2 (as opposed to z_1 for the other currents) because the initial 12mA scan was taken at slightly different initial position. However, this does not affect the comparison of the models since the $G_n(x)$ and $G_m(y)$ contributions are tabulated as percentages.

Modal Index n	$G_n(x)$ content at position z_2	$G_n(x)$ content at position z_2+10μm	$G_n(x)$ content at position z_2+20μm	$G_n(x)$ content at position z_2+30μm	Average	Standard deviation as a % of the mean
0	25.2%	23.7%	20.9%	17.8%	21.9%	14.9%
1	67.5%	61.0%	61.6%	63.3%	63.4%	4.6%
2	7.3%	15.2%	17.5%	17.9%	14.5%	34.1%
3	0.0%	0.0%	0.0%	0.0%	0.0%	0.0%
4	0.0%	0.0%	0.0%	0.0%	0.0%	0.0%
5	0.0%	0.0%	0.0%	1.1%	0.3%	200.0%

Table 6.7: Modal content in x for I = 12mA.

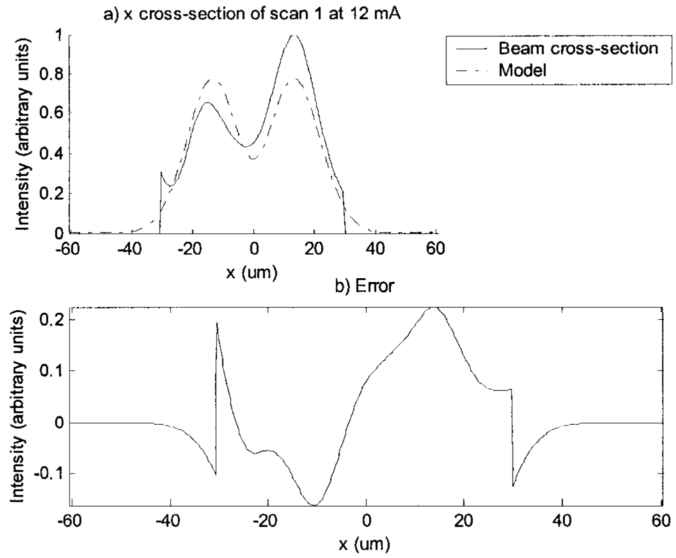

Figure 6.7: cross-section of the beam and the evaluated model for z-position z_2. b) The error was computed by subtracting the cross-section and the model.

Modal Index m	$G_m(y)$ content at position z_2	$G_m(y)$ content at position z_2+10μm	$G_m(y)$ content at position z_2+20μm	$G_m(y)$ content at position z_2+30μm	Average	Standard deviation as a % of the mean
0	28.4%	27.4%	27.0%	26.2%	27.3%	3.4%
1	68.6%	70.6%	70.9%	71.9%	70.5%	2.0%
2	0.0%	0.0%	0.0%	0.0%	0.0%	0.0%
3	2.8%	0.0%	0.0%	0.0%	0.7%	200.0%
4	0.1%	2.0%	2.1%	1.8%	1.5%	62.8%
5	0.0%	0.0%	0.0%	0.0%	0.0%	0.0%

Table 6.8: Modal content in y for I = 12mA.

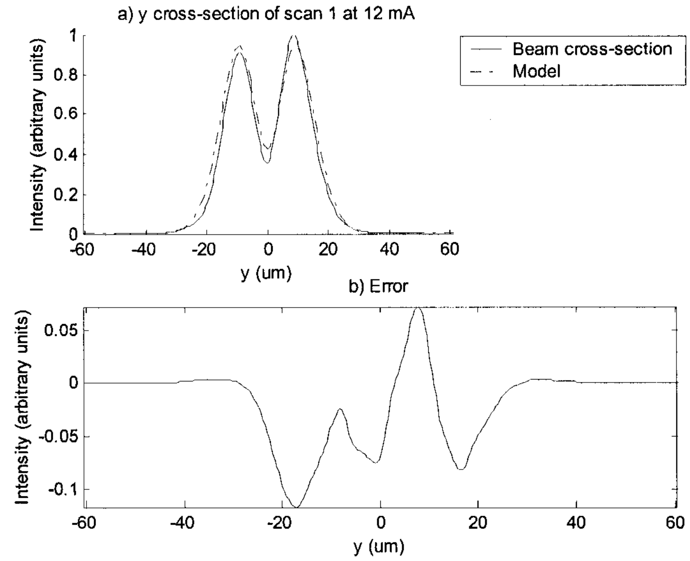

Figure 6.8: cross-section of the beam and the evaluated model for z-position z_2. b) The error was computed by subtracting the cross-section and the model.

The results at 12mA show a greater variation than for the other currents. Because the beam has grown in width due to the larger contribution of high order modes it surpassed the scanning range of the SNOM. Therefore the beam was clipped during the beam sampling process.

The preceding results indicate that a consistent one-dimensional model can be computed for the VCSEL at multiple output currents. Thus, the choice of beam waists in x and y, as well as the orientation of the basis axes appear to be sufficiently accurate. The tables in this section contain the standard deviation as a percentage of the mean. This measurement helps quantify the stability of the sampling and modeling process for different z-positions. It is observed that the deviation for the dominant basis functions is small. Determination of the non-dominant basis functions is less accurate. This will not have significant effect on the model because the contribution of those functions to the overall model is small.

6.2.2 Integration method

As was stated in Chapter 4, the integration method reduces the intensity to a one transverse dimensional function by integrating it in x or y. Thus all the modes whose modal coefficient (c_{nm}) share a common index (n or m if integration is done in x or y respectively). Therefore, if it is desired to examine the intensity in the x-dimension, the intensity profile is integrated in y and is reduced to equation 4.6 reprinted below for convenience.

$$I(x,z_1) = \int_{-\infty}^{\infty} \sum_{m=0}^{\infty}\sum_{n=0}^{\infty} c_{nm} \left|u_{nm}(x,y,z_1)\right|^2 dy = \sum_{n=0}^{\infty}\left(\left|G_n(x,z_1)\right|^2 * \sum_{m=0}^{\infty} c_{nm} \right) \qquad \text{(Eqn 4.6)}$$

The individual modes can not be distinguished, only the summed values are seen. However, the M^2 factor can be evaluated. Table 6.9 tabulates the percentage that each $G_n(x)$ makes to the total power of the beam. The values in the table are the average of the values found at the four z-positions for each current. Table 6.10 contains the data for the y dimension. The values of I = 12mA were excluded because the severe beam clipping prevented an accurate model from being evaluated.

Current (mA)	Modal Content n = 0	Modal Content n = 1	Modal Content n = 2	Modal Content n = 3	Modal Content n = 4	Modal Content n = 5	M^2_x
4	64.6%	22.1%	8.2%	3.4%	1.3%	0.4%	2.12
5	59.2%	26.3%	9.8%	3.4%	1.1%	0.1%	2.23
10	46.5%	31.9%	16.3%	5.1%	0.1%	0.0%	2.61

Table 6.9: The percentage of each $G_n(x)$ to the beam's power.

Current (mA)	Modal Content m = 0	Modal Content m = 1	Modal Content m = 2	Modal Content m = 3	Modal Content m = 4	Modal Content m = 5	M^2_y
4	90.6%	0.0%	7.9%	0.5%	1.0%	0.0%	1.43
5	55.7%	36.55	3.0%	2.6%	1.3%	0.8%	2.19
10	31.5%	38.0%	18.7%	7.5%	2.5%	1.7%	3.33

Table 6.10: The percentage of each $G_m(y)$ to the beam's power.

From the tables it is observed that the values for M^2_x and M^2_y are not the same. This is expected since the contributions of the $G_n(x)$ and $G_m(y)$ basis functions are not the same and the beam is not perfectly circular. The value of M^2 increases with current as the higher order modes begin to lase and the laser spot size increases.

6.2.3 Two transverse dimensional method

In order to determine the modal content it is necessary to perform the analysis using basis functions in x and y. From the preceding sections it was found that it becomes increasingly difficult to model the beam with HG functions as the current increases. The two transverse dimensional model fails to produce meaningful results once the non-symmetry in the beam becomes very pronounced. The best result was obtained for I = 4mA. The modal content is tabulated in table 6.11.

Mode (n,m)	Modal Content	Mode (n,m)	Modal Content	Mode (n,m)	Modal Content
(0,0)	55.1	(3,1)	0.8	(4,4)	0.0
(0,1)	0.0	(2,3)	0.0	(0,5)	0.3
(1,0)	20.8	(3,2)	0.6	(5,0)	0.5
(1,1)	0.0	(3,3)	0.0	(1,5)	0.0
(0,2)	2.2	(0,4)	0.0	(5,1)	0.6
(2,0)	7.9	(4,0)	1.3	(2,5)	0.0
(1,2)	2.1	(1,4)	0.3	(5,2)	0.2
(2,1)	0.5	(4,1)	0.8	(3,5)	0.0
(2,2)	1.2	(2,4)	0.1	(5,3)	0.1
(0,3)	0.8	(4,2)	0.3	(4,5)	0.0
(3,0)	3.3	(3,4)	0.1	(5,4)	0.0
(1,3)	0.0	(4,3)	0.1	(5,5)	0.0

Table 6.11: Modal content for I = 4mA at position z_1.

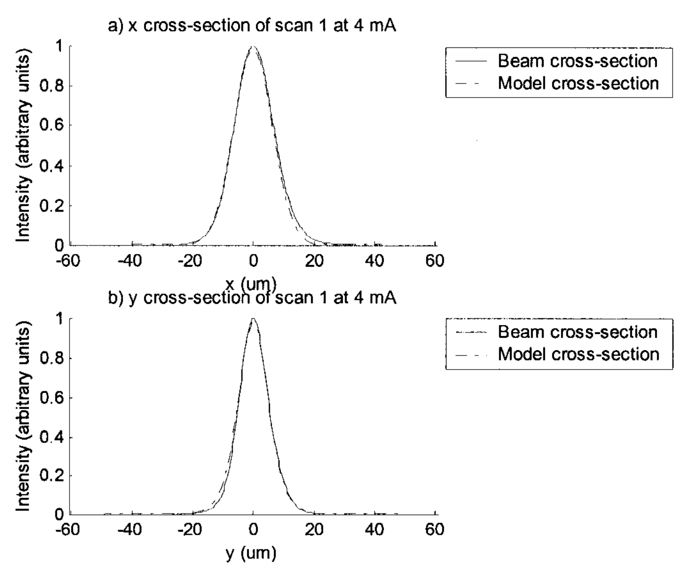

Figure 6.9: Comparison of the cross-sections of beam and the evaluated model in (a) x and (b) y.

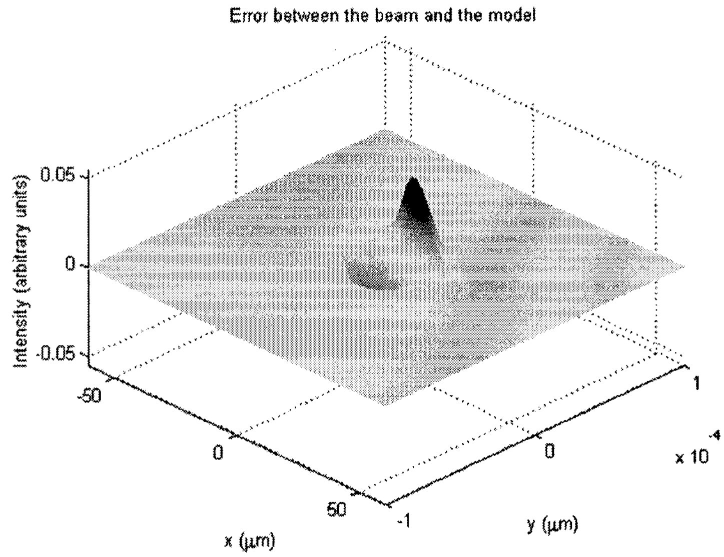

Figure 6.10: Difference of the actual beam and the model.

The values for the M^2 factor in x and y were found to be $M^2_x = 2.48$ and $M^2_y = 1.45$. The values in table 6.11 can be reduced to values close to those in tables 6.9 and 6.10 by summing the modes with m in common for x and n in common for y. In the ideal case the values would be identical. The values of M^2 computed by both methods should be very close (identical if the beam was ideally HG). Comparing to the value in tables 6.9 and 6.10 for I = 4mA, it is found that there is a good agreement between the values of M^2_y, but the two M^2_x have a 17% difference. The model contains 98.5% as much power as the real beam.

Axis	Modal Content n = 0	Modal Content n = 1	Modal Content n = 2	Modal Content n = 3	Modal Content n = 4	Modal Content n = 5	M^2
x	58.30	23.16	9.75	4.86	2.57	1.33	2.48
y	88.90	2.73	6.54	1.00	0.53	0.30	1.45

Table 6.12: The percentage of each $G_n(x)$ or $G_m(y)$ to the beam's power.

6.3 Conclusion

This chapter demonstrated that the VCSEL under study could be modeled by Hermite-Gauss functions for low currents. As the current is increased the beam becomes corrupted by non-HG elements which hinder modal extraction and make it impossible to accurately model the beam using purely HG functions. The integration and cross-sectional methods provided limited models of the beam in one transverse dimension. These models were stable as the beam propagated in free space. The two transverse dimensional method returns the modal content of the beam. If the VCSEL emissions are very close to ideally HG, as was the case for I = 4mA (section 6.2.3) this model will be accurate and will allow for the determination of the beam's evolution with distance as it propagates through an optical system.

6.4 References

[1] C. Degen, B. Krauskopf, G. Jennemann, I. Fischer., W. Elsaber, "Polarization selective symmetry breaking in the near-fields of vertical cavity surface emitting lasers", J. Opt. B: Quantum Semiclass. Opt. Vol. 2, No. 4, 2000, pp. 517-525.

[2] F. Gori, M. Santarsiero, "Intensity-based modal analysis of partially coherent beams with Hermite-Gaussian modes", Optics Letters, Vol. 23, No. 13, July 1998, pp. 989-991.

[3] M. Santarsiero, F. Gori, R. Borghi, G. Guattari, "Evaluation of the modal structure of light beams composed of incoherent mixtures of Hermite-Gaussian modes", Applied Optics, Vol. 38, No. 25, September 1999, pp. 5272-5281."Evaluation of the modal structure of light beams composed of incoherent mixtures of Hermite-Gaussian modes", Applied Optics, Vol. 38, No. 25, September 1999, pp. 5272-5281.

7. Modal extraction using a two-lens system

7.1 Introduction

In Chapter 5, SNOM was used to measure the intensity profiles of a VCSEL. This method produces high quality images. Another method is to image the beam waist using a lens relay system and to acquire the intensity profiles using an optical probe mounted on an x-y-z stage or a CCD camera [1,2,3,4,5,6]. The addition of lenses into the experimental setup will introduce distortion into the imaged beam which will interfere with beam analysis. In addition the imaging system will be diffraction limited. However, there are some benefits to creating a new beam waist. The probe will be able to scan through the position corresponding to the imaged beam waist. This will make it possible to measure the beam evolution in free space and will increase the accuracy of the determination of ω_0 using the method described in section 4.9 [7].

The intent of the experiments in this chapter was to evaluate the modal content using a two-lens relay system and compare the performance of the lens relay system to that of the SNOM. A different VCSEL was used than in the previous chapters. The device used was in a 20x16 array with device spacing equal to 125μm (figure 7.1). Only one VCSEL in the array was used. The experiments in this chapter were performed before the SNOM equipment became available. It was expected that it would be of greater difficulty to evaluate the modal content from these experiments because of distortion introduced by the lens system. The advantage of this system is that it had a much larger x-y-z range than the SNOM which allowed for intensity profiles to be measured at more z-positions. Although the two-lens system modifies the laser beam and creates a new beam waist neither the modal content nor the value of the M^2 factor is changed by the optical system.

Figure 7.1: The VCSEL array and the first lens in the lens relay system.

7.2 VCSEL properties

The wavelength of the VCSEL emissions is 850nm. The I-V and L-I curve plotted in figures 7.2 and 7.3 respectively. The threshold current is I_{th} = 1.35mA and the slope efficiency is η = 0.25mW/mA. The beam is only reasonably symmetric in x. There is a significant variation in beam shape in y which suggest anisotropy in the VCSEL cavity [3]. For this reason the modeling process will only be performed on a cross-section along the x-axis using the method presented in section 4.4. The other two methods will not produce useful information due to the lack of symmetry.

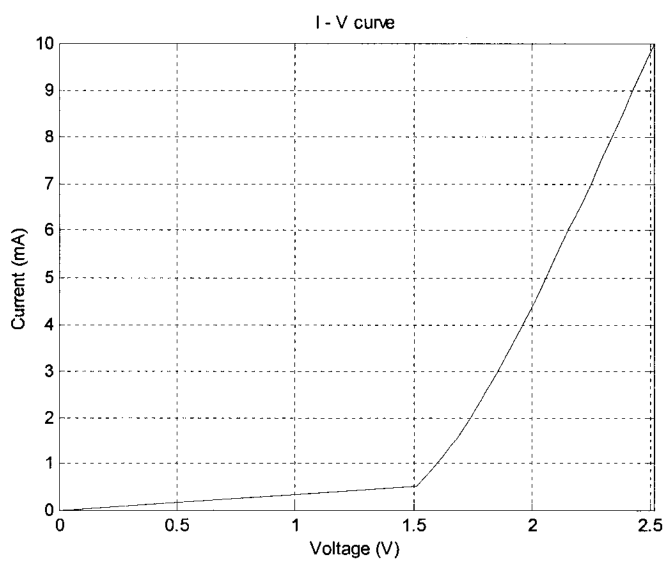

Figure 7.2: Current vs. voltage.

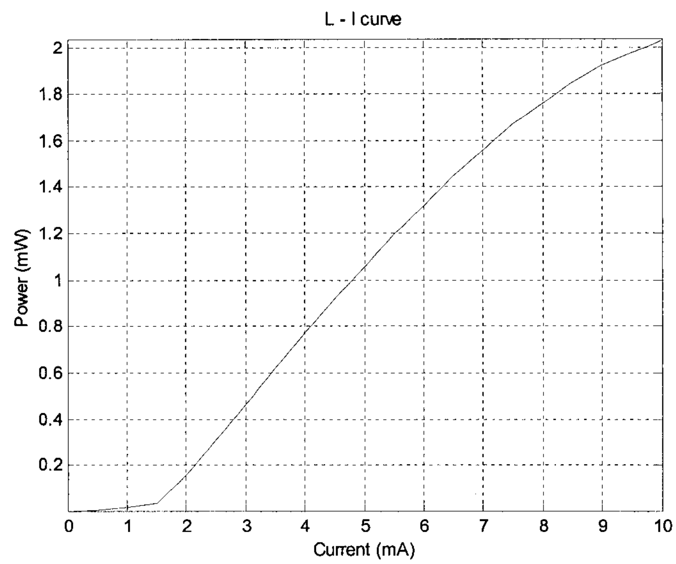

Figure 7.3: Power vs. current.

7.3 Evaluation of the M^2 factor and the modified beam waist ω_0'

The setup depicted by figure 7.4 was used to measure the variance of the beam from which the M^2 factor and beam waist radius ω_0' can be computed. A new beam waist was created by refocusing the laser beam through a two-lens system. The first lens was a microscope objective with magnification of 10. The second lens was a plano-convex doublet with focal length equal to 30mm and diameter equal to 12.5mm. When a lens relay is used it must be determined if the properties of the optical system will distort the beam in a manner that will result in an erroneous model. Issues that must be addressed are misalignment, clipping and power transmission. To align the system components the propagation of the beam through the system was verified by measuring the beam profile and position at several points in the system and comparing to the expected results. For example if the beam's center is not on the optical axis at all points in the system this can indicate that the surface of the VCSEL is not perpendicular to the optical axis of the lens relay or that the center of the beam waist is not exactly on the optical axis. To address beam clipping, the focal lengths of the lenses and the component spacing were chosen to produce spots on the surface of the lenses which were small enough to avoid beam clipping. Furthermore, the absence of Airy disk patterns, which are introduced when a beam diffracts through a circular aperture, suggests that no significant beam clipping occurred. Only 40% of the power was transmitted through the system due to reflections at the lens surfaces, but no significant distortion was observed in the output of the lens relay. Thus despite the power loss the modal content of the beam is unchanged and can be evaluated.

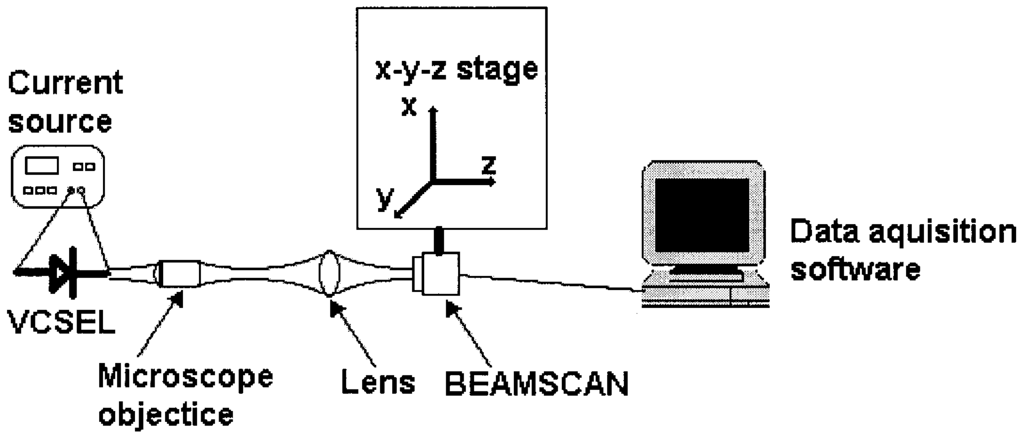

Figure 7.4: Schematic of the setup used to measure the variance of the beam in order to evaluate M^2 and ω_0.

The device in figure 7.5 at the output of the lens relay is used to measure the variance of the beam. The M^2 factor was evaluated for currents of 2.0, 2.5, 2.8, 3.5 and 5mA using the method presented in section 4.10. Figure 7.6 is a plot of the measured beam variance and the results of the M^2 calculations are tabulated in table 7.1. As is expected the value of M^2 increases with current which indicates the increase in higher order modes and the corresponding increase in beam size [8]. The variance data was used to compute the beam waist radius parameter, $\omega_0' = 4.5\mu m$, of the modified beam which was then used to evaluate the beam radius at the positions for which the model is found in the following section (section 7.4).

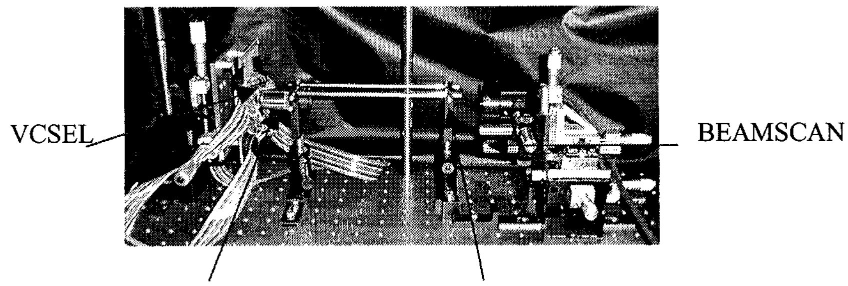

Figure 7.5: A new beam waist is created by the 2-lens system. The BEAMSCAN device at the output of the second lens is used to measure the variance of the modified beam.

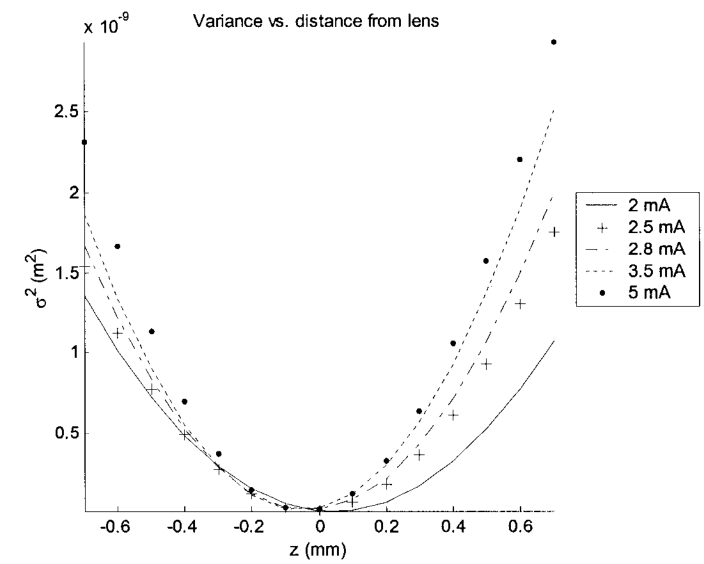

Figure 7.6: The variance was sampled at 15 z-positions around the beam waist. The z-distance is measured from the location of the new waist.

Current I (mA)	M^2
2.0	2.81
2.5	3.94
2.8	4.45
3.5	4.93
5.0	4.96

Table 7.1: The value of the M^2 factor is found from the variance curves in figure 7.6.

7.4 Modal extraction

The setup depicted in figure 7.7 was used to acquire the x cross-section of the beam. The beam-profiling device was removed from the system and replaced with a photo-detector mounted on a motorized x-y-z stage. A 10μm pinhole was placed on the photo-detector in order to sample only a small part of the beam at any point. A scan is performed at a fixed y and z to obtain the cross-section of the beam by sampling the intensity at points along the x-axis. The profile was then reconstructed from the acquired data. Profiles were obtained for several z-positions and currents. The following section compares the models for scans at I = 2.5, 2.8 and 3.5mA. In this section, two scans are presented per current, corresponding to positions z = 1 and 1.5mm from the new beam waist. It is expected that the value of the computed percentage of any $G_n(x)$ will be very close for the two z-positions since modal content remains constant as the beam propagates.

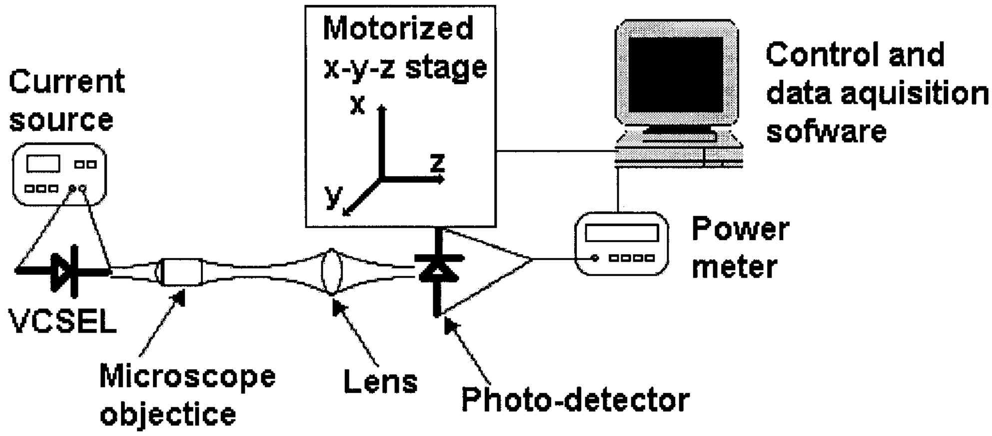

Figure 7.7: The setup used to measure the VCSEL emission.

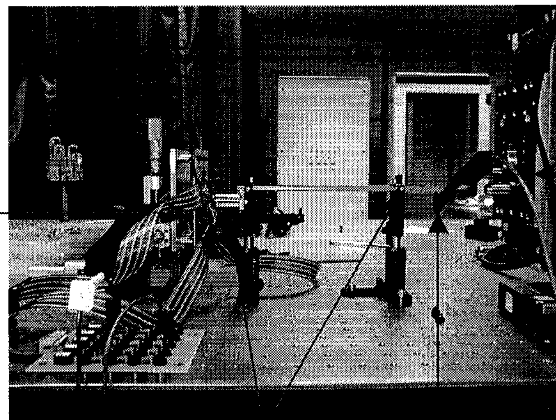

Figure 7.8: The setup used to acquire the intensity cross-section along the x-axis.

Table 7.2 tabulates the model for I = 2.5mA. Figure 7.9 plots the x cross-section of the actual beam and the difference between the two for z = 1mm. The intensity profiles have been normalized to a maximum intensity of 1 so that the error between the beam and its model is plotted as fraction of 1. As was the case in chapter 6, the error curve is non-symmetric about x = 0 because while the model is symmetric the actual beam is not ideally HG and not perfectly symmetric. The percentage of the $G_n(x)$'s for the two z-positions are relatively close.

z (mm)	$G_n(x)$ Content n = 0	$G_n(x)$ Content n = 1	$G_n(x)$ Content n = 2	$G_n(x)$ Content n = 3	$G_n(x)$ Content n = 4	$G_n(x)$ Content n = 5
1	0.0	47.5	44.7	7.8	0.0	0.0
1.5	0.0	46.2	42.8	11.1	0.0	0.0

Table 7.2: The model of the beam at I = 2.5mA, as computed at z = 1 and 1.5mm.

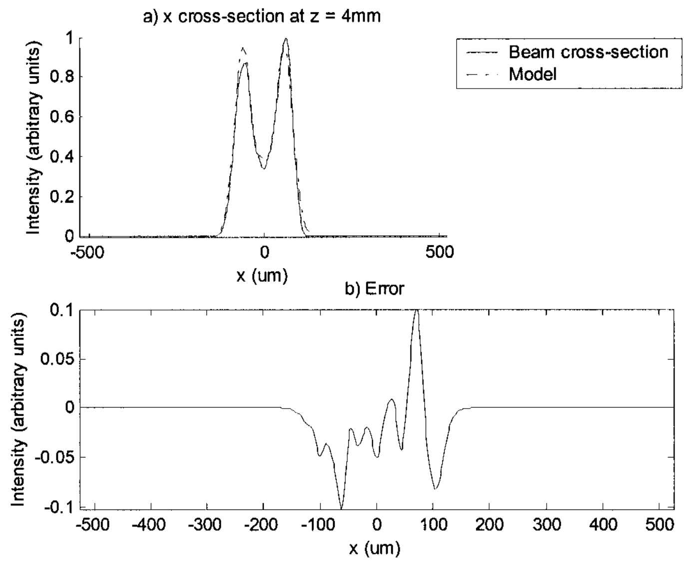

Figure 7.9: a) x cross-section of the beam and the evaluated model for z-position 1mm. b) The error was computed by subtracting the cross-section and the model.

Table 7.3 tabulates the model for I = 2.8mA. Figure 7.10 plots the superposition of the model and the actual beam and the difference between the two for z = 1mm. With the increase in current the contribution of the higher modes becomes more pronounced.

z (mm)	$G_n(x)$ Content n = 0	$G_n(x)$ Content n = 1	$G_n(x)$ Content n = 2	$G_n(x)$ Content n = 3	$G_n(x)$ Content n = 4	$G_n(x)$ Content n = 5
1	0.0	35.9	47.3	16.9	0.0	0.0
1.5	0.0	34.2	43.7	19.1	3.0	0.0

Table 7.3: The model of the beam at I = 2.8mA, as computed at z = 1 and 1.5mm.

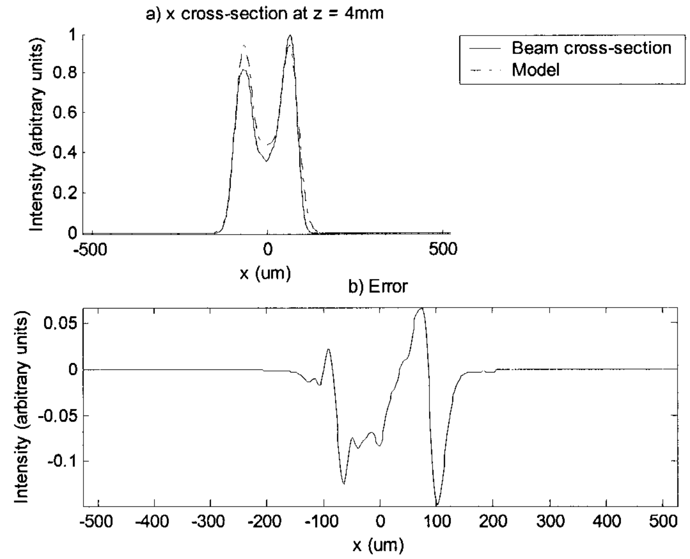

Figure 7.10: a) x cross-section of the beam and the evaluated model for z-position 4mm. b) The error was computed by subtracting the cross-section and the model.

Table 7.4 tabulates the model for I = 3.5mA. Figure 7.11 plots the superposition of the model and the actual beam and the difference between the two for z = 1mm. The output of the VCSEL used in this experiment remained relatively similar in shape over the range in current examined.

z (mm)	$G_n(x)$ Content n = 0	$G_n(x)$ Content n = 1	$G_n(x)$ Content n = 2	$G_n(x)$ Content n = 3	$G_n(x)$ Content n = 4	$G_n(x)$ Content n = 5
1	0.0	31.6	48.9	19.6	0.0	0.0
1.5	3.3	27.6	38.1	24.8	6.1	0.0

Table 7.4: The model of the beam at I = 3.5mA, as computed at z = 1 and 1.5mm.

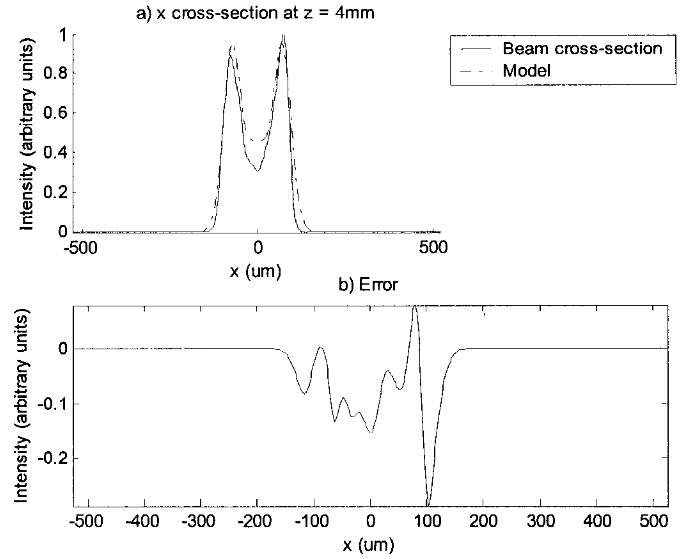

Figure 7.11: a) x cross-section of the beam and the evaluated model for z-position 1mm. b) The error was computed by subtracting the cross-section and the model.

7.5 Conclusion

In this chapter a two-lens system was used to create a new beam waist so that the variance of the beam could be measured directly at the beam waist. This information allowed the computation of the M^2 factor and the evaluation of the beam waist radius parameter ω_0. A model of the cross-section of the beam was evaluated using ω_0 to define the $G_n(x)$ basis functions. The ability to scan through the position of the waist (section 7.3) simplified the determination of ω_0 and M^2 from the variance compared to the SNOM experiments. The larger range of the x-y-z stage used in this setup prevented the beam clipping which occurred for large beam sizes with the SNOM. However, it was much more difficult to align the system due to the larger number of components. The resolution of the probe used to acquire the intensity profiles (section 7.4) was poor compared to that of the SNOM probe because the size of the pinhole was 10μm. For this reason it was necessary to measure the beam at a distance of about 1mm or greater from the imaged beam waist in order to get an accurate profile. This obstacle could be overcome by using a smaller aperture on the photo-detector used. Nevertheless, it is clear that the resolution of the measurements that can be acquired with SNOM is far superior to those using a lens relay system and this will in turn result in a more accurate model for the beam.

7.6 References

[1] T. Ackemann, S. Barland, M. Cara, S. Balle, J.R. Tredicce, R. Jager, M. Grabherr, M. Miller, K.J. Ebeling, “Spatial mode structure of bottom-emitting broad-area vertical-cavity surface-emitting lasers”, J Opt B Quant Semiclassical Opt, Vol. 2, No. 3, 2000, pp. 406-412.

[2] D.L. Boiko, E. Le Cren, G.M. Stéphan, P. Besnard, “Spectrum of vertical-cavity surface-emitting lasers: linewidth properties and non-degeneracy of relaxation oscillation frequencies”, J. Opt. B: Quantum Semiclass. Opt., Vol. 3, No. 2, April 2001, pp. S166-S172.

[3] C. Degen, B. Krauskopf, G. Jennemann, I. Fischer., W. Elsaber, “Polarization selective symmetry breaking in the near-fields of vertical cavity surface emitting lasers”, J. Opt. B: Quantum Semiclass. Opt. Vol. 2, No. 4, 2000, pp. 517-525.

[4] C. Degen, I. Fischer, W. Elsaber., "Transverse modes in oxide confined VCSELs: Influence of pump profile, spatial hole burning, and thermal effects", Optics Express, Vol. 5, No. 3, August 1999, pp. 38-47.

[5] M.I. Cohen, A.D. Rakic, M.L Majewski, “Phase retrieval methods for the determination of transverse mode structure in vertical-cavity surface-emitting lasers”, Optoelectronic and Microelectronic Materials And Devices Proceedings, 1996 Conference on , 1996, pp. 67 –70.

[6] V.E. Boros, A.D. Rakic, M.L. Majewski, “Measurement automation for characterising vertical cavity surface emitting lasers”, Optoelectronic and Microelectronic Materials Devices, 1998. Proceedings. 1998, Conference on , 1999, pp. 392 –395.

[7] Xin Xue, Andrew G. Kirk, "Methods for estimating beam parameters of super-imposed Hermite-Gaussian modes", Optics in Computing 2000, Proc. SPIE - Int. Soc. Opt. Eng, vol.4089, 2000, pp. 829-835.

[8] A.E. Siegman, S.W. Townsend, "Output Beam Propagation and Beam Quality from a Multimode Stable-Cavity Laser", IEEE Journal of Quantum Electronics, Vol. 29, No. 4, April 1993, pp. 1212-1217.

8. Conclusions

The intent of this project was to model the output of a VCSEL beam using the method developed by Gori et al. under the assumption that the intensity profile could be accurately represented using Hermite-Gauss modes. The purpose of computing a model is that it will allow the prediction of the beam evolution through an optical system with greater accuracy than other methods such as M^2. To achieve this the Gori et al. method was applied to VCSELs whose outputs could be best characterized by Hermite-Gauss functions at certain currents. The cross-sectional method and integration methods described in Chapter 4 produced accurate models of the beam for several currents. As was stated previously, the models that were computed varied slightly with the change in z-position along the optical axis. This was due to several factors such as slight misalignment in the measurement system or small variations in the VCSEL output with time. For data measured with the SNOM, the cross-sectional method produced models which did not deviate greatly with z distance along the optical axis. For example for $G_n(x)$'s whose content was 50% or greater of the model, the standard deviation due to the change in z was less than 5%. The standard deviation for $G_n(x)$'s whose content was less than 1% was greater than 100% in some cases. However, since the contributions of these modes are so small the model remains accurate. These models provided information on the beam shape and modal content, but could not isolate the individual modes in the output. Based on these models the modeling process was performed using the two-transverse dimensional method in order to extract the modal content. It was found that the VCSEL output could be effectively modeled at a current of 4mA because its output was strongly Hermite-Gauss. However, the exact modal content could not be obtained for larger currents because the VCSEL's output became increasingly non-symmetric.

Two experimental setups were used to acquire the intensity profiles. The SNOM setup proved to be superior to the two-lens system. It provided a much higher resolution image of the intensity and was significantly faster. The alignment of the SNOM to the VCSEL is more accurate than for the lens system. Only the SNOM probe must be aligned to the VCSEL surface. In the lens relay system, the two lenses and the probe must be aligned.

Perfect alignment of either system is not possible, but the greater number of elements in the lens system resulted in greater distortion of the intensity profile. The added accuracy of the SNOM is required to obtain consistent models because the acquired data is being mathematically decomposed into basis functions. Small distortions introduced by the measurement setup can result in erroneous determination of the modal content.

There are several issues that arose during the course of this project which suggests the possibility of future work. The application of the two-transverse dimensional modeling method to the experimentally acquired VCSEL output proved to be difficult. The limiting factors were the quality of the VCSEL output, i.e. the VCSEL did not emit a perfectly Hermite-Gauss beam, and the experimental setup that was used to acquire the intensity profiles. Possible future work would involve developing a mathematical representation of this output. This would require the use of additional functions which would be non Hermite-Gauss, to model the non-symmetric elements in the output. However, it must be determined if these non-symmetric elements can be represented with orthogonal functions. If they can not, then a unique solution for the modeling process may not be possible.

Another possible future project would be the implementation of a feedback mechanism in the SNOM setup. This would result in greater accuracy because it would maintain a constant probe height above the VCSEL. This would also allow for the probe to be safely placed closer to the VCSEL surface. The smaller mode-field diameter near the surface of the VCSEL would eliminate the clipping of the beam which occurred at high currents, such as 12mA (Chapter 6), thus allowing for a larger range of currents to be modeled.

The significant amount of research on VCSELs suggests that they will continue to play a role in future optical systems. Advances in VCSEL technology will ensure further study of VCSEL's characteristics such as their structure, performance and their modal content.